The Egyptian Journal of Remote Sensing and Space Sciences 25 (2022) 941–960

HOSTED BY

Contents lists available at ScienceDirect

The Egyptian Journal of Remote Sensing and Space Sciences

journal homepage: www.sciencedirect.com

Research Paper

Multiscale mineralogical investigations for mineral potentiality mapping of Ras El-Kharit-Wadi Khashir district, Southern Eastern Desert, Egypt

Hatem M. El-Desoky [a], Ali Shebl [b,c,*], Ahmed M. Abdel-Rahman [a], Wael Fahmy [a], Hamada El-Awny [a], Anas M. El-Sherif [d], Mahmoud M. El-Rahmany [a], Árpád Csámer [b]

[a] *Geology Department, Faculty of Science, Al-Azhar University, PO Box 11884, Nasr City, Cairo, Egypt*
[b] *Department of Mineralogy and Geology, University of Debrecen, 4032 Debrecen, Hungary*
[c] *Department of Geology, Tanta University, 31527 Tanta, Egypt*
[d] *Faculty of Engineering, Northern Border University, KSA*

ARTICLE INFO

Article history:
Received 18 April 2022
Revised 7 August 2022
Accepted 11 September 2022
Available online 11 October 2022

Keywords:
Sentinel 2
ASTER
Hydrothermal alteration
Ore mineralogy
Eastern desert

ABSTRACT

Through various scales of observation, ranging from remote sensing data, field investigations, hand specimens, microscopic petrographic examinations, XRD, to SEM, indicators of various mineralization types are highlighted in Ras El-kharit-wadi Khashir (Eastern Desert, Egypt). Systematic remote sensing exploration of the mineralized zones is performed through integrating Sentinel 2 and ASTER datasets. False-color combinations, informative band ratios, relative absorption band depth, and CEM techniques were applied to discriminate rock units and various types of hydrothermal alterations. Moreover, ALOS PALSAR DEM was utilized to decipher the structural lineaments. Intensive field investigations confirmed hydrothermally altered zones that were picked out through remote sensing analysis and revealed that the study area is affected by cataclastic metamorphism to some extent. Magmatic and metamorphic rock types are represented by propylitic, phyllic, argillic, and silicification zones. Sericitization, chloritization, epidotization, kaolinitization, carbonatization, and silicification are recorded utilizing petrographic and remote sensing investigations. Moreover, the current study reveals that the detected alteration is the main reason for the apparent wide range of petrographic characteristics of each rock type and bearing several opaque minerals, such as pyrite, magnetite, titanomagnetite, chalcopyrite, arsenopyrite, covellite, galena, goethite, and hematite. Most of these opaques were identified using ore microscopy, XRD, and SEM. The distribution of hydrothermal alterations, representative samples bearing mineralization, structurally dissected zones are integrated to build a mineral potentiality map of the study area. The resultant MPM was confirmed via field survey and emphasized the usefulness of the current integrated approach besides highlighting about 125 km^2 as potential mineralized zones.

1. Introduction

The Precambrian complex of the Egyptian shield is divided into five basic rock units from oldest to youngest: (1) metamorphic rocks (gneisses and migmatites), (2) dismembered ophiolites, (3) arc-volcanic/volcaniclastic metasedimentary units, (4) Hammamat molasse type sediments and Dokhan volcanic sequences, and (5) granitic rocks (Hamimi et al. 2019). Stern and Hedge (1985) classified the Egyptian Eastern Desert into three parts: the Northern, Central, and South-Eastern Deserts (NED, CED, and SED), which all exhibit various features of the region and intensive Neoproterozoic event of magmatic activity and deformation. According to Fig. 1a the studied region, situated between the two shear zones (Kharit-Hodien and South Hafafit suture), was highly influenced by these two orogenies, resulting in the establishment of many shear zones. Greiling et al. (1994); Greiling et al. (1996) postulated the South Hafafit Suture (SHS) (Fig. 1a), which identified SSW-wards thrusting directly to the south of the Hafafit complex. Concerning Kennedy (1964) generally, the study area is thought to be affected by two types of metamorphism: (a) high-grade regional metamorphism affected on metasediments during the pre-Pan-African Hafafit Orogeny (630–600); (b) slightly and locally low grade – greenschist facies – metamorphism affected on volcaniclastic rocks during Pan-African tectono-thermal events (600–450 Ma). El-Kazzaz (2010) suggested Wadi Ras El-Kharit region is covered by two separate rock types associated with two different

---

* Corresponding author at: Department of Mineralogy and Geology, University of Debrecen, 4032 Debrecen, Hungary.

E-mail address: ali.shebl@science.tanta.edu.eg (A. Shebl).

https://doi.org/10.1016/j.ejrs.2022.09.001
1110-9823/

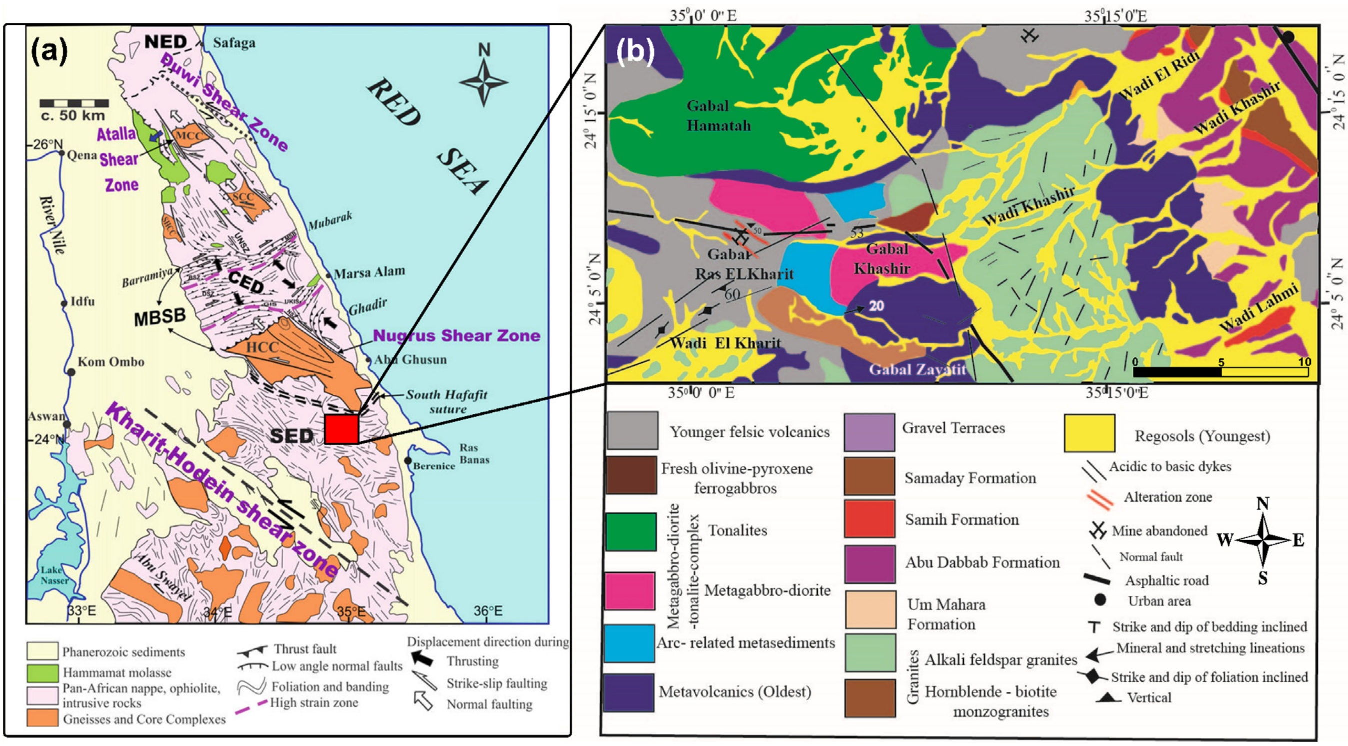

Fig. 1. **(a)** Tectonic map of the Central and South Eastern Desert, including the study area between Kharit-Hodein shear zone in the south and South Hafafit suture. SED; South Eastern Desert, CED; Central Eastern Desert, NED; Northern Eastern Desert, NSZ, Nugrus shear zone, UNSZ, Um Nar shear zone, HCC; Hafafit Core Complex, SCC; Sibai Core Complex; MCC; Meatiq Core Complex; and MBSB, Mubarak–Baramiya shear belt. This map is compiled from Greiling et al. (1994), Fritz et al. (1996), de Wall et al. (2001) and (Abd El-Wahed 2014). **(b)** Detailed geologic map of Wadi Khashir - Gabal Ras El-Kharit district (Modified after EGSMA, 1997).

orogenies (Fig. 1b): volcaniclastic series and igneous intrusions from the Pan-African orogeny (600–450 Ma), and high-grade metasediments from the pre-Pan-African Hafafit Orogeny (>600 Ma).

Geological mapping and mineral exploration in the traditional sense are labor-intensive, expensive, and time-consuming. On the contrary, modern exploration approaches (mainly utilizing remote sensing datasets), save time, effort, and help to separate potential areas from non-interesting areas for further exploration (Rajesh, 2004). The capability of remote sensing in lithological mapping and identification of related hydrothermal mineralization has been demonstrated by several studies (Ramadan et al., 2001; Gad and Kusky, 2006; Zhang and Pazner, 2007; Goetz 2009; Gabr et al., 2010; Azizi et al., 2010; Salem and Soliman, 2015; Abdelmalik, 2019; El Ghrabawy, et al. 2019; Farag et al., 2019; Zoheir, et al. 2019; Fowler et al., 2020; Nguemhe Fils et al., 2020; Wambo et al., 2016, 2020; Traore et al., 2020; El-Desoky, 2021;Abd El-Wahed et al., 2021; Shebl and Csámer, 2021c; Ketchaya et al., 2021; Fossi et al., 2021; Mbianya et al., 2021; Shebl and Csámer, 2021a; El-Hadidy et al., 2022).

For the exploration and exploitation of mineral resources, reliable geosciences information in the form of geological and mineralogical potential maps is crucial. Consequently, integrated remote sensing satellite data with laboratory techniques is a quick and cost-effective way for detecting hydrothermal zones for mineral development (Lamri et al., 2016). During hydrothermal processes, changes in rock composition, mineralogy, and texture can result in the formation of various alteration zones that extend for kilometers in vertical and lateral directions. Through its extent (sensed through moderate to high spatial resolution satellites), and according to the applied techniques and the utilized sensor, the hydrothermal alteration zones could not only be detected but also specified and classified. Consequently, the current study applied Sentinel 2 and ASTER data sets due to their reasonable spatial and spectral resolutions for geological applications to highlight various types of hydrothermal alterations and their closely related minerals that could guide to favorable zones of mineralization when combined with structural elements and verified via field survey petrographic examinations and ore mineralogy.

2. Geological setting

The study district is about 400 km^2 between longitudes 35° 00′–35° 30′E and latitudes 24° 05′–24° 15′N according to WGS84

Table 1
Characteristics of ASTER and Sentinel 2 data.

ASTER			Sentinel 2		
Band	**Central wavelength (μm)**	**Spatial resolution (m)**	**Band**	**Central wavelength (μm)**	**Spatial resolution (m)**
1	0.560	15	1	0.443	60
2	0.660	15	2	0.490	10
3N	0.820	15	3	0.560	10
3B	0.820	15	4	0.665	10
4	1.650	30	5	0.704	20
5	2.165	30	6	0.740	20
6	2.205	30	7	0.782	20
7	2.260	30	8	0.842	10
8	2.330	30	8a	0.865	20
9	2.395	30	9	0.945	60
10	8.291	90	10	1.375	60
11	8.634	90	11	1.610	20
12	9.075	90	12	2.190	20
13	10.657	90			
14	11.318	90			

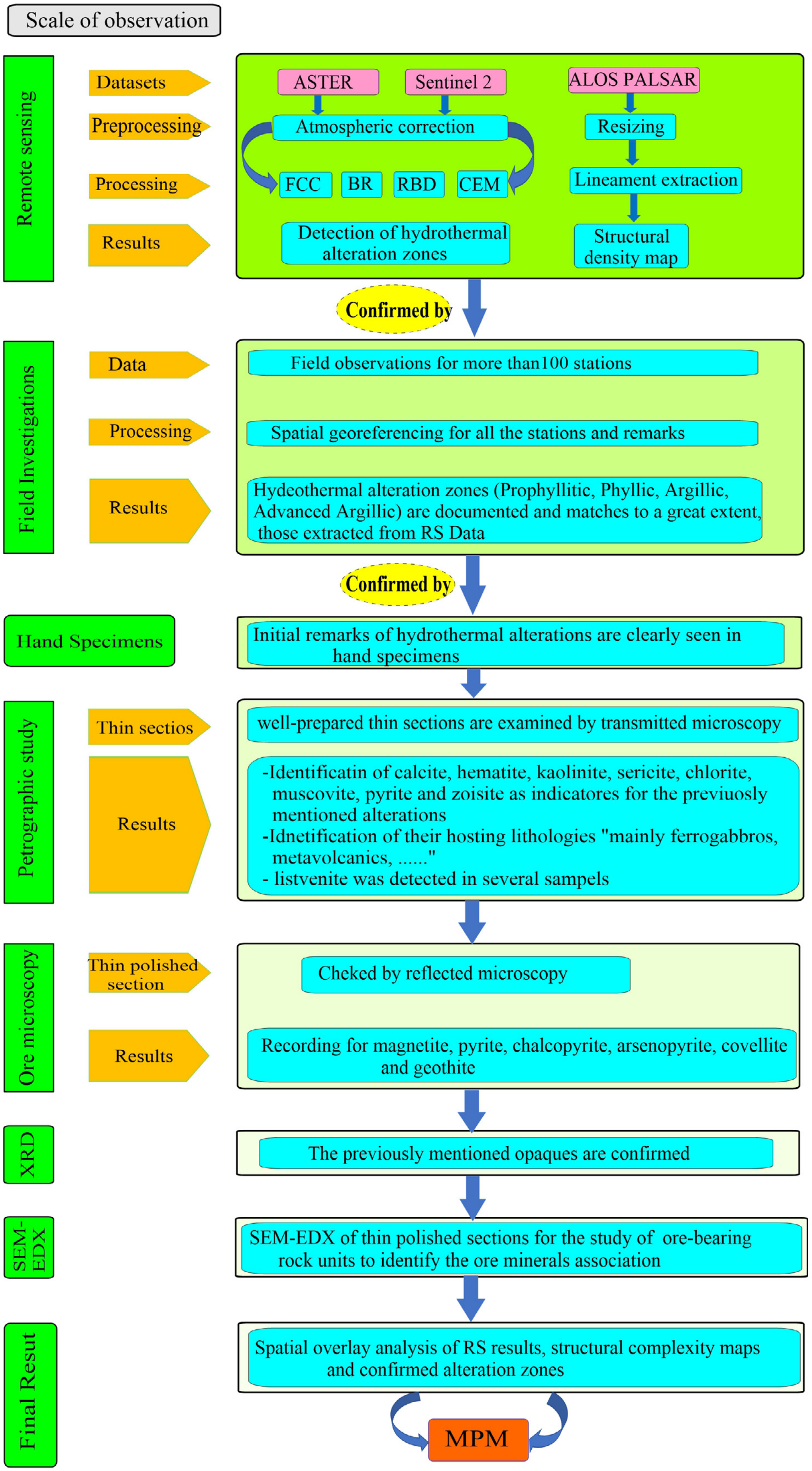

Fig. 2. A flowchart demonstrating the utilized methodology combining remote sensing data and laboratory studies.

Datum and UTM zone 36 N Projection (Fig. 1). This region consists of Egyptian Nubian Shield rocks from the Hamata area in the central section of the South-Eastern Desert (Fig. 1a, b). Geomorphologically, the study area comprises several mountains which grading in height such as Gabal Hamata (1862 m), Gabal Khashir (1560 m), Gabal Ras El-Kharit (1560 m), Bir Hamata (565 m) and

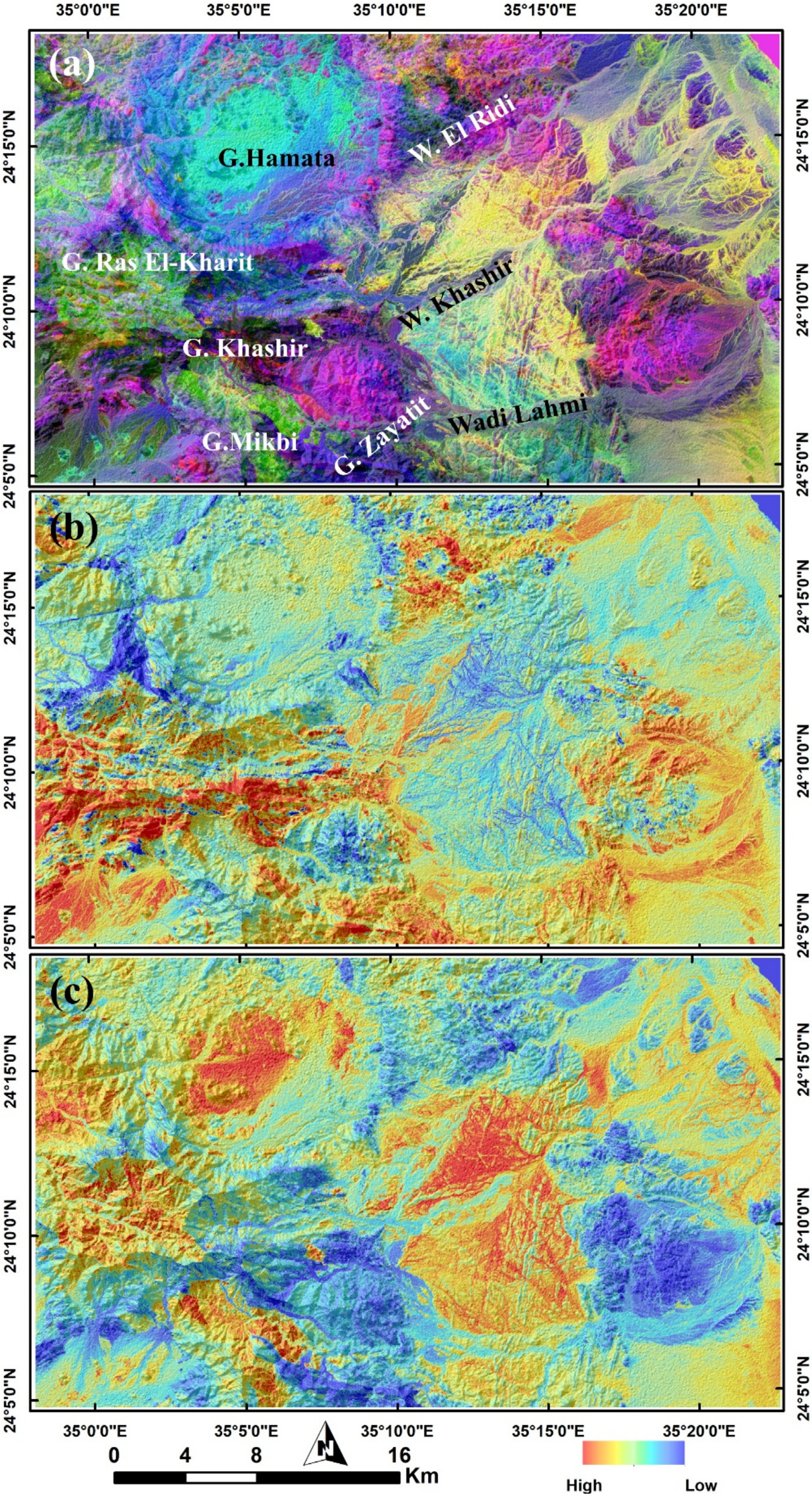

Fig. 3. (a) Sabins' band ratio combination respectively in RGB, (b) Ferrous iron, and (c) Ferric iron minerals in the study area.

Gabal Mikbi (1410 m). The present area is characterized by the basement complex (igneous and metamorphic rocks) overlaid by Phanerozoic rocks of the Samaday and Samih formation.

Based on the field observation, mode of occurrence and geological mapping, the basement rock units at the study district comprises of metavolcanics, arc-related metasediments, metagabbro-

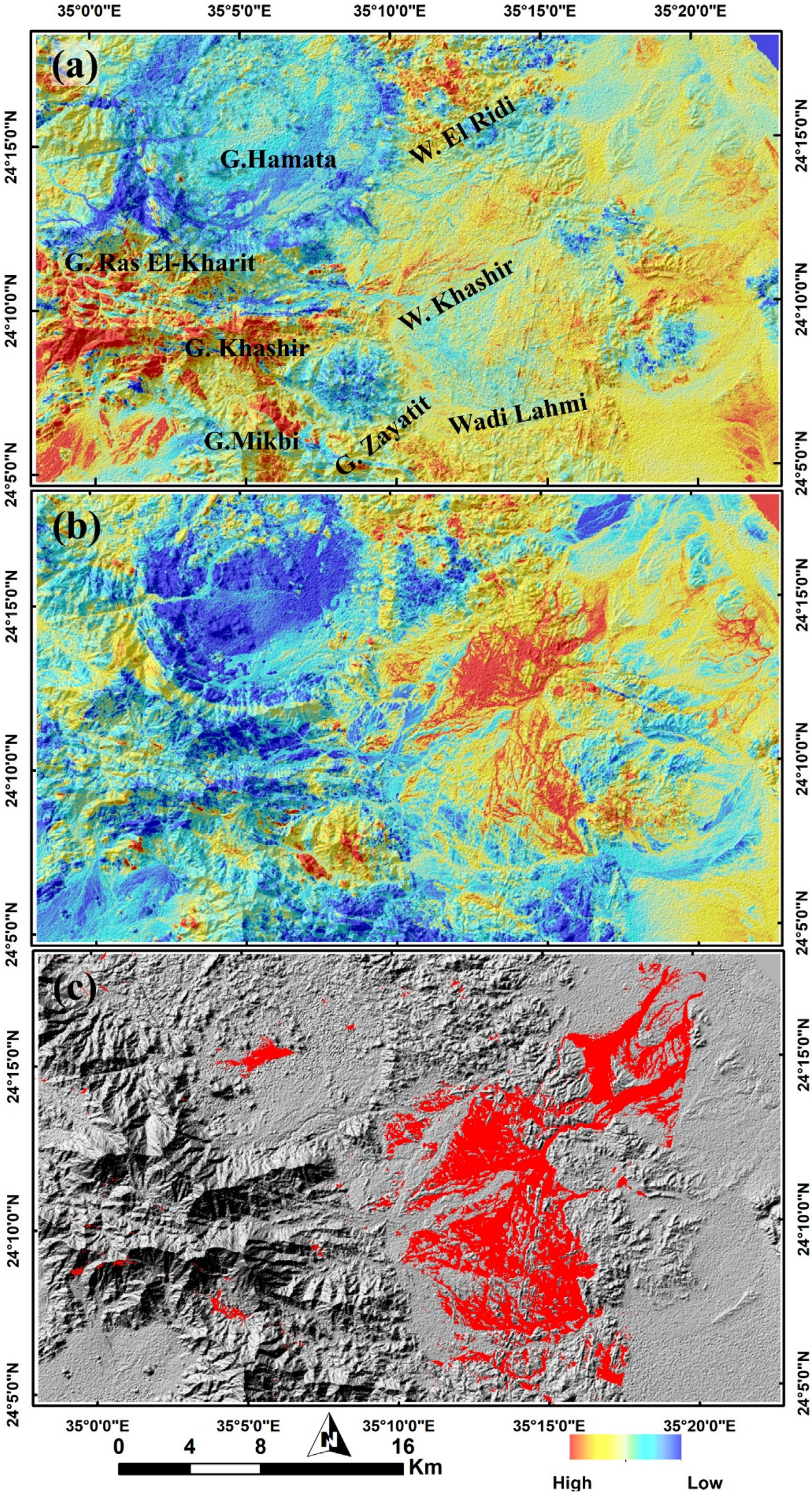

Fig. 4. Pseudocolor ramps showing (a) Gossan, and (b) hydroxyl-bearing minerals utilizing Sentinel 2 data and (c) confirmed OH-bearing minerals using ASTER data.

diorite-tonalite complex, fresh olivine-pyroxene ferrogabbros, younger felsic volcanics, alkali feldspar granites, monzogranite, and different types of dykes covered by red sandstones (Fig. 1).

Wadi Khashir metavolcanics includes *meta*-andesites and listvenites. On the other hand, Gabal Ras El-Kharit metavolcanics are represented by metabasalts. Listvenites are mostly carbonated

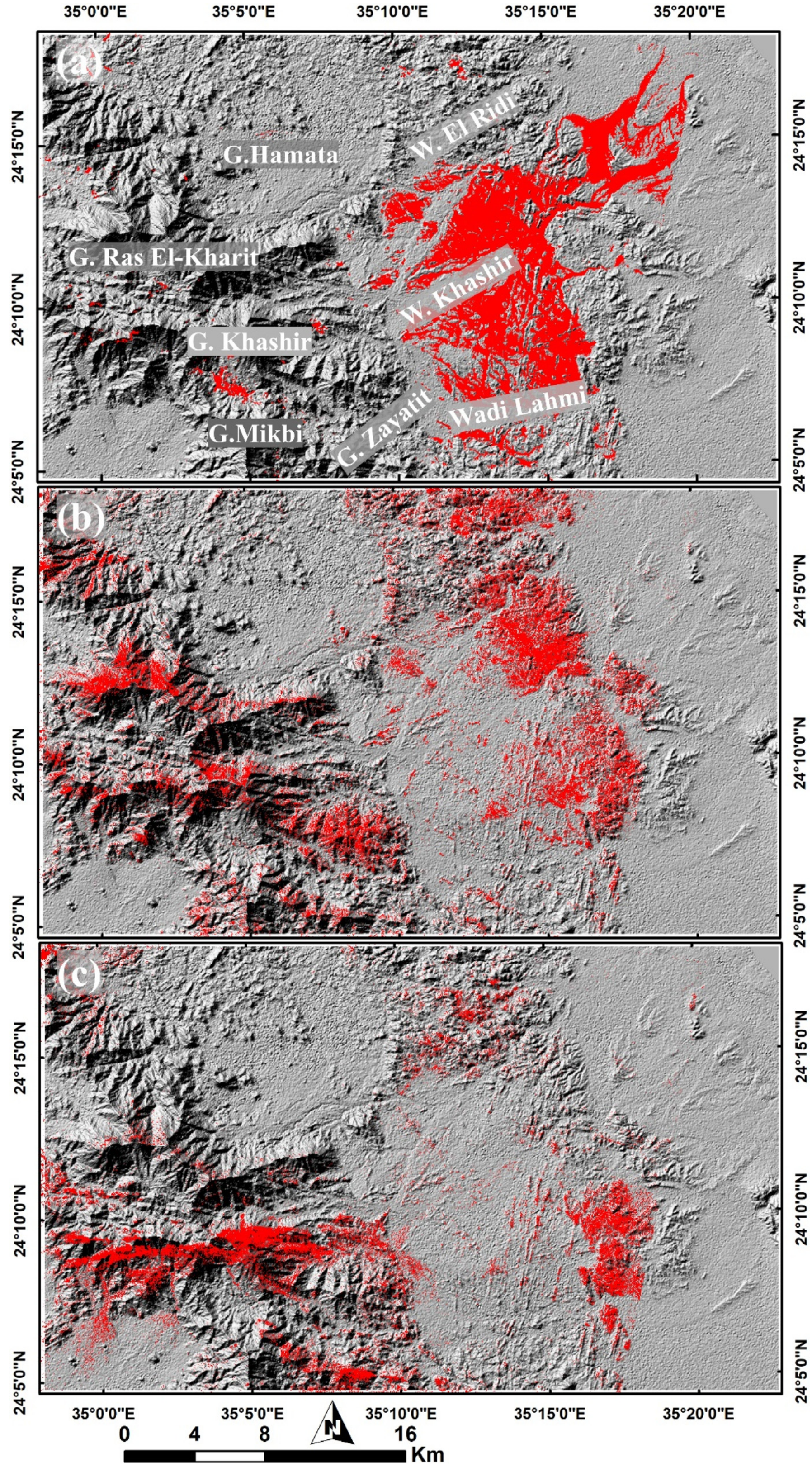

Fig. 5. Distribution of (a) advanced argillic, (b) argillic-phyllic alteration anomalies, and (c) chlorite/calcite/epidote based on ASTER data.

with a little proportion of quartz. The oxidation of Fe-bearing carbonate to iron oxides is responsible for the reddish-brown surface appearance. Listvenites were detected along the shear zone in metavolcanics at Wadi Khashir as a result of hydrothermal solution invasion.

The field observation indicates that the arc-related metasediments in the investigated district are younger than the proper metavolcanics. It exhibits a fine- to medium-grained character, with columnar or vertical joints and well-developed lineation, and displays in brownish, greyish, dark greenish-grey, and black colors. The mineral content of these metasediments significantly differs from each other. Quartz-pyroxene schists, pebbly-quartz-biotite schists, mylonitic schists, and quartzites are among them.

The western side of Wadi Khashir is covered by metagabbro-diorite-tonalite rocks. Metagabbro is mainly composed of medium- to coarse-sized plagioclase, pyroxene, hornblende, quartz, and olivine, and sometimes forms spheroidal weathered masses. Diorites are comprised mostly of plagioclase, quartz, and pyroxene and are medium to coarse-grained, light grey to greenish-grey in color. These rocks are often highly jointed, fractured, and tectonized, with NE-E trends of 80°. Tonalites are medium to coarse-grained, whitish-grey in color, and have a granular texture with xenoliths and mafic mineral alignment.

Ferrogabbros rocks are recorded in the western portion of Wadi Khashir. They show medium to coarse-grained, dark greyish to dark greenish in fresh surface color, and occasionally speckled in white. Some ore minerals, such as magnetite and pyrite crystals, can be observed in these rocks. The younger felsic volcanic rocks cover a large area from Wadi Khashir and Gabal Ras El-Kharit district. These rocks are sheared, fractured, and include highly ferruginated rhyolites as well as altered rhyolites on occasion. The alteration zones along sheared mineralized rhyolites range in thickness from 5 to 20 m and extend to roughly a kilometer, bearing pyrite, chalcopyrite, goethite, and hematite, among other ore minerals.

Wadi Khashir and Gabal Ras El-Kharit are bordered by granites. The granitic pluton of Wadi Khashir stretches from east to west (15 km in length). The western portion of Gabal Ras El-Kharit granitic pluton intruded into the younger felsic volcanic rocks. These rock units are classified to two types: hornblende-biotite monzogranites and alkali feldspar granites. The hornblende-biotite monzogranites form an oval pluton-like shape. They are very weathered, with low to moderate topographic relief, and are greatly altered and broken. The alkali feldspar granite is encountered in the western portion of the Wadi Khashir area. Two structural dykes, basic and acidic ones, govern the emplacement of alkali feldspar granitic plutons in the examined region. The red beds of sandstones from the Samaday Formation cover the geological sequence revealed in the eastern half of Wadi Khashir.

3. Materials and methods

3.1. Remote sensing datasets

In the current research, Sentinel 2 and ASTER datasets were integrated to configure the hydrothermal alteration pattern within the study area. Sentinel 2 is a multispectral sensor that provides

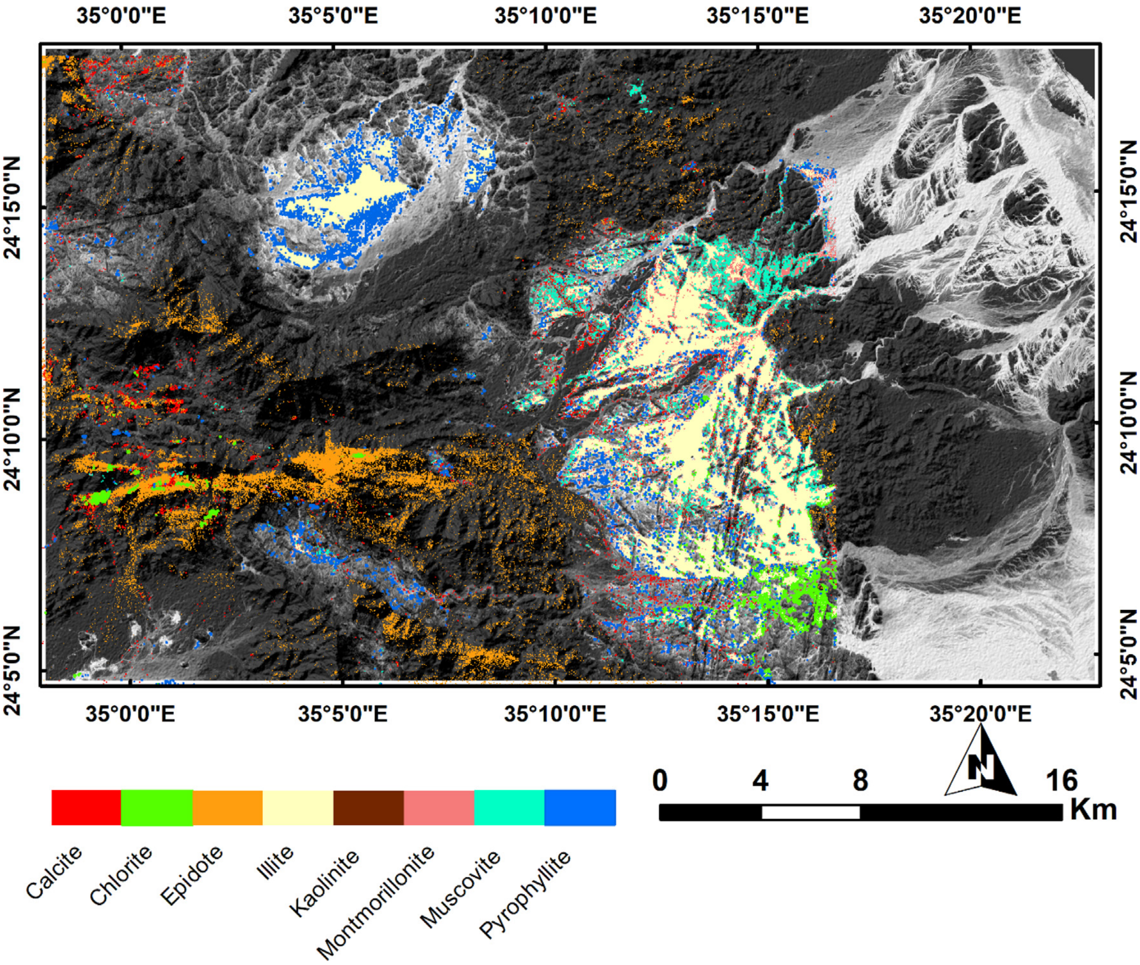

Fig. 6. CEM findings (distribution of seven minerals commonly associated with different types of alteration) over a grey scale image of the study area.

global coverage with spatial resolution up to 10 m. Through 13 spectral bands spanning VNIR and SWIR regions (Table 1), reasonable lithological discrimination and hydrothermal alteration detection could be achieved by utilizing Sentinel 2 data. For specification of various types of alterations, ASTER data was incorporated in the current research due to its thoroughgoing SWIR coverage. ASTER

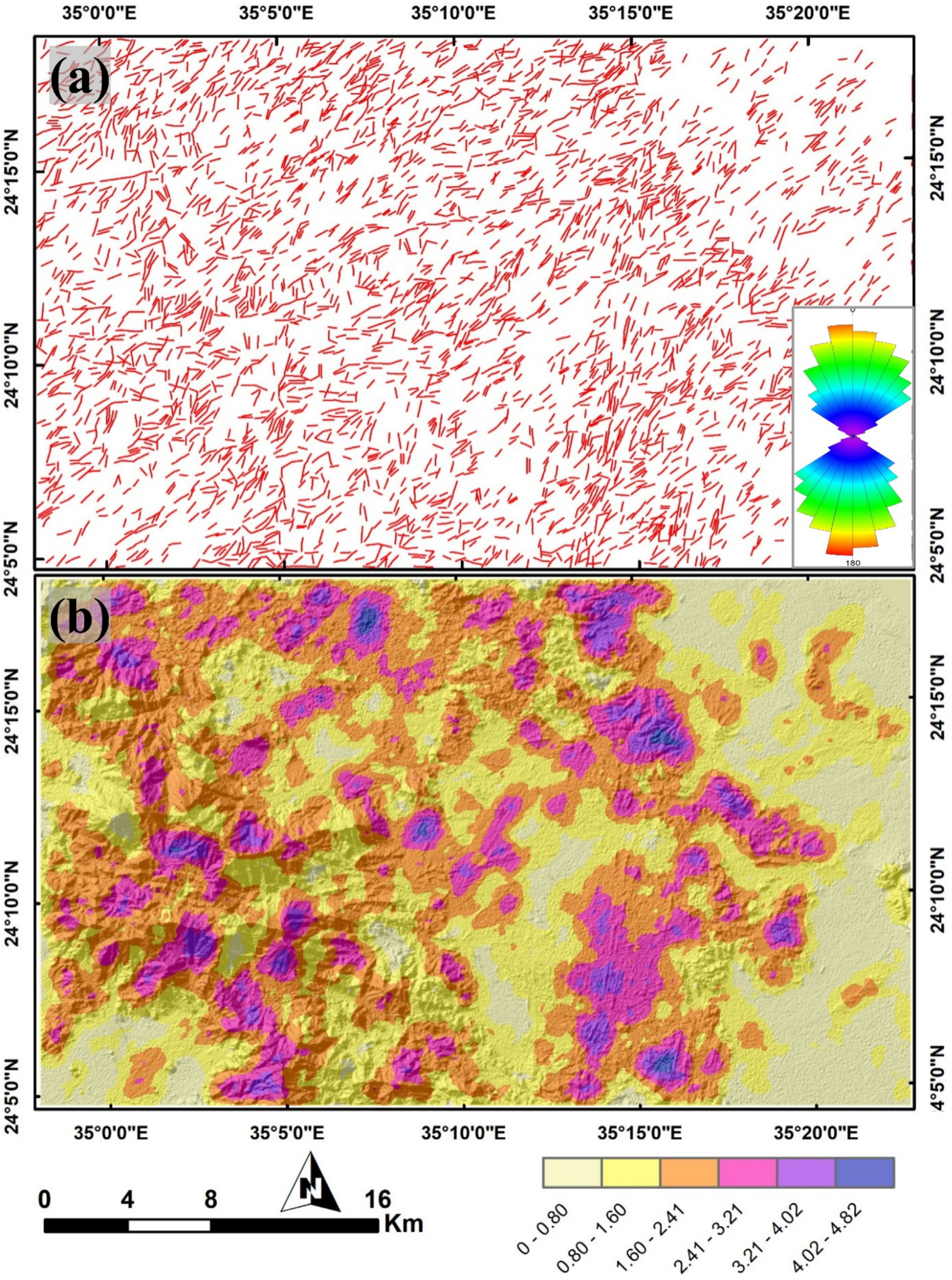

Fig. 7. (a) Lineaments extracted automatically from PALSAR DEM and rose diagram for the study area; (b) lineaments density map.

was launched in 1999, however, it is extensively used in geological studies due to its reasonable covering of VNIR (15 m pixel size), SWIR (30 m), and TIR (90 m) regions as shown in Table 1. Toward the aim of the current study, Sentinel 2 and ASTER scenes were accessed, geometrically projected, radiometrically corrected, and handled by utilizing SNAP and QGIS. Besides using FCCs for comprehensive lithological differentiation, several image processing techniques including band ratios (BR), relative absorption band depth (RBD), and Constrained Energy Minimization (CEM) were applied to ASTER and Sentinel 2 data to allocate various types of hydrothermal alteration and their index minerals.

Besides hydrothermal alterations, structural elements have a great role in outlining several mineralization occurrences. To automatically delineate the lineaments within the study area, ALOS PALSAR DEM was implemented due to its efficacy in extracting linear features compared to other widely used optical datasets (Shebl and Csámer, 2021b). PCI Geomatica LINE module was applied to detect edges and link the resultant lines through assigning filter radius, edge gradient threshold, curve length threshold, line fitting threshold, angular difference threshold, and linking distance threshold as 10, 50, 30, 3, 15, and 20, respectively. These values deliver the best results considering the dominant structural trends within the study area. Additionally, they were previously used over similar terrains and their results were effective and comparable with structural complexity resulting from aeromagnetic data (Shebl et al., 2021).The integration of digital processing of Sentinel 2 and ASTER data and laboratory analysis are presented in the given flowchart (Fig. 2).

3.2. Field evidence and analytical techniques

Using a global positioning system (GPS) survey, more than 100 rock samples were collected from lithological units and alteration zones. Thin section preparation (for examination in transmitted light), polished thin section (for examination in reflected light), X-ray diffraction (XRD) examination, and scanning electron microscope (SEM) investigations are all part of the laboratory analysis. The mineral compositions, textures, and alteration types of the investigated rocks of 50 thin sections of rock samples were petrographically analyzed - under a polarized microscope. Ore microscopy on polished thin sections, X-ray diffraction (XRD), and Scanning Electron Microscopy with Energy Dispersive X-ray Analyses (SEM-EDX) techniques were used to identify the ore textures and components. SEM-EDX analyses were carried out on ore minerals in all samples using SEM Model Quanta 250 FEG (Field Emission Gun) attached with EDX Unit (), at the Central Laboratories of the Egyptian Mineral Resources Authority (EMRA). The accelerating voltage was 30 kV, the magnification ranges from 14 × up to 1.000.000×, while the resolution for the gun was 1 nm.

4. Results

4.1. Remote sensing results

Through variations in spectral reflectances, identification of several functional groups (e.g., carbonate, hydroxyl, etc.) could be

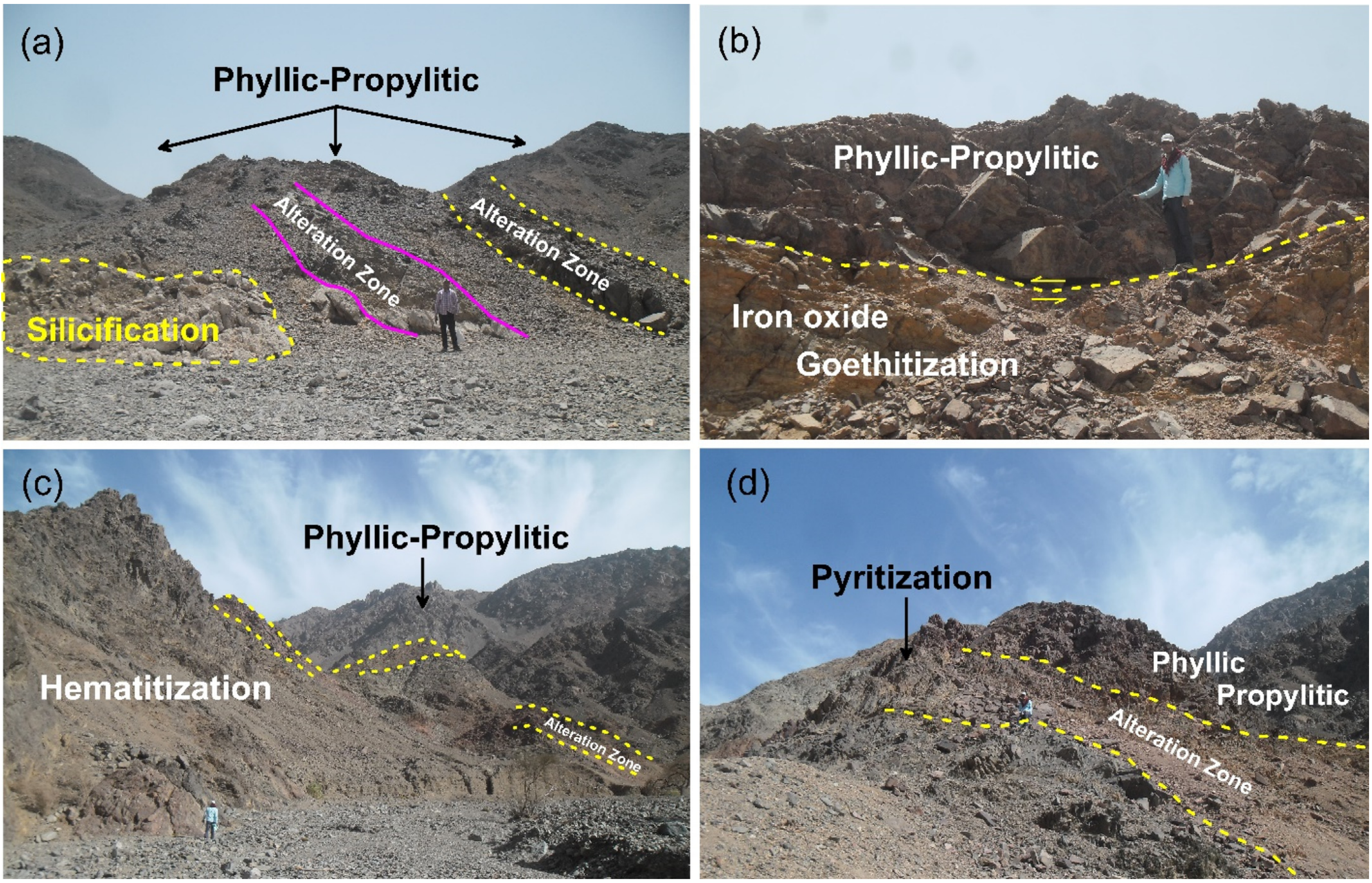

Fig. 8. Field observations. **(a)** Silicification zone associated phyllic-propylitic- alteration with metavolcanic rocks. **(b)** View of oxidation zone (geothite and pyrite) contacted with in the younger felsic volcanics (rhyolites). **(c & d)** The iron oxides (hematite-pyrite) associated alteration zone.

achieved. These spectral variations could be highlighted to disclose several hydrothermal alteration minerals through various image processing techniques. As well-known methods, specific Band ratios and RBD (Aboelkhair et al., 2010; Emam et al., 2016; Shebl et al., 2021) were applied to ASTER and Sentinel 2 data to configure the hydrothermal alteration pattern within the study area.

The general distribution of hydrothermal alterations is accomplished by Sabins ratio (Sabins, 1999) FCC applied to Sentinel 2 data. It highlights hydroxyl-bearing minerals (b11/b12) in red, iron oxides (b4/b2) in green and ferrous iron oxides (b4/b11) in blue as shown in Fig. 3a. Then, further inspection of ferrous iron (b12/b8), ferric iron (b4/b3), gossan (b11/b4), and hydroxyl-bearing minerals (b11/b12) is carried out by utilizing Sentinel 2 data as shown in Fig. 3b, 3c, 4a, and 4b, respectively. To check and confirm Sentinel 2 results, the hydroxyl-bearing minerals were additionally extracted using the ASTER band ratio (b4/b9) as shown in Fig. 4c. By using the two sensors, the distribution of the extracted hydroxyl-bearing minerals clearly demonstrates how well the

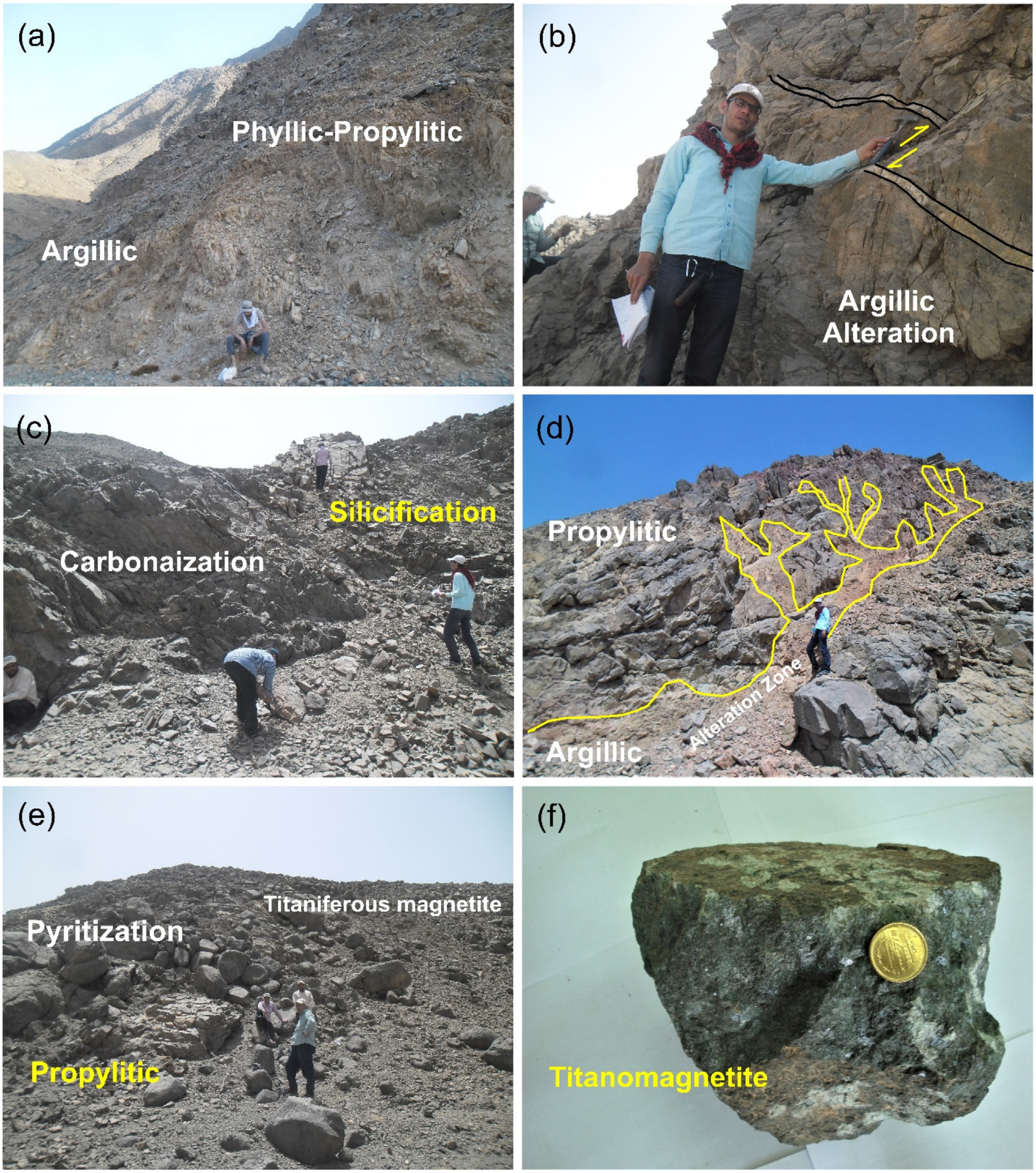

Fig. 9. Field photographs of the hydrothermal alteration types in the study area. **(a)** View of the argillic- phyllic-propylitic alteration zone in metasediments rocks (quartz-biotite schists). **(b)** Argillic alteration along fault plane of quartz vein within monzogranites. **(c)** Carbonate and silica alteration associated listvenite rocks. **)d)** Altered zone permeates metabasalt-related propylitic and argillic alteration**. (e)** Titaniferous magnetite mineralization along propylitic and pyrite zone in ferrogabbro rocks. **(f)** Close view of titanomagnetite mineralization in a hand specimen.

matching is. It should be emphasized that each sensor of the utilized datasets has its own advantageous characteristics that could help in achieving our target. For instance, ASTER did not cover the bluish spectrum range (included in Sentinel 2, around 0.48 nm) which is extremely useful in specifying iron accompanying alteration (extracted in the current study using Sentinel 2); however, it is extremely useful in specifying various types of alterations e.g., phyllic, argillic, etc., due to the detailed SWIR coverage compared to Sentinel 2 data. According to spectral characteristics of ASTER data and making the best use of the narrow SWIR coverage, advanced argillic (b4/b6) and argillic-phyllic (b5/b6) alterations were assigned, as shown in Fig. 5a and 5b. Then, the general distribution of chlorite/calcite/epidote (Fig. 5c) was extracted through RBD (b7 + b9)/b8). More closely to the alteration index minerals, the CEM technique was applied to ASTER data utilizing USGS spectral library to highlight calcite, chlorite, epidote, muscovite, kaolinite, pyrophyllite, and illite (Fig. 6). The integrated results (from the two sensors) are extremely useful in delineating the whole alteration pattern within the study area as Sentinel 2 largely contributes to detecting for example ferrous, ferric, gossan, etc., alterations and ASTER could powerfully detect and reasonably discriminate hydroxyl bearing minerals.

Structural analysis results clearly show that the study area is intensively dissected through linear features (Fig. 7a). Visual interpretation of the detected lineaments revealed that these linear features include faults, dykes, and joints cross over most of the lithological units and possess NW-SE and NE-SW dominant trends. The western side of the study area is rather dissected compared to the eastern part which is mainly covered by sedimentary rocks. Due to the importance of these linear features in controlling hydrothermal fluids, a lineament density map (Fig. 7b) was built to highlight the highly fractured zones, which are considered of

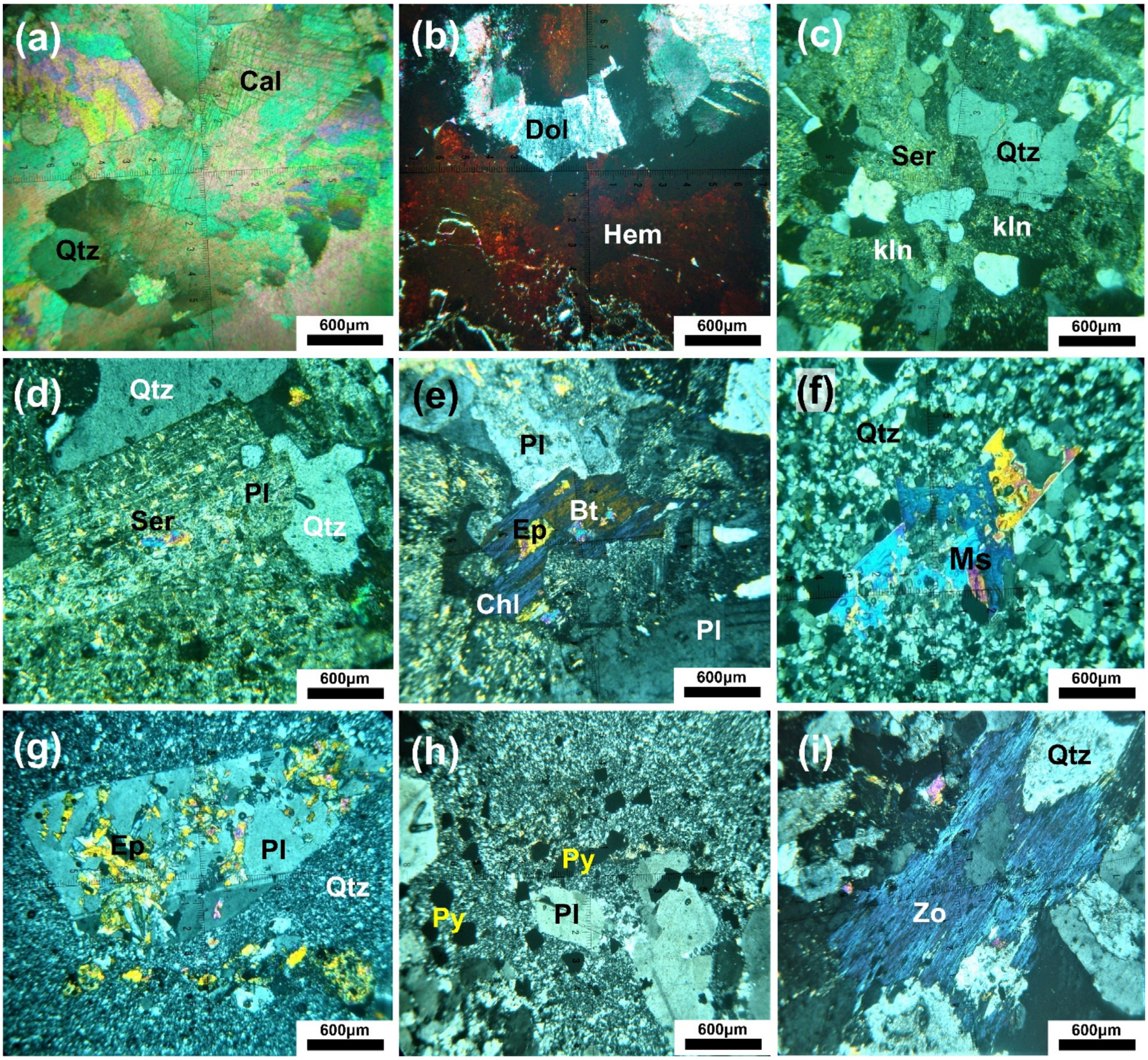

Fig. 10. Microphotographs of alteration rock samples (a)Silicification (Qtz) and Carbonization (Cal) crystals in listvenite rocks along propylitic zone.(b)Propylitic-oxidation zone (Dolomitization and hematitization) in listvenite.(c) Sericite (Ser) and kaolinite (Kln) of plagioclase (Pl) crystals in alkali feldspar granites associated argillic/phyllic zone.(d) Highly altered of plagioclase (Pl) to sericite (Ser) in alkali feldspar granites (Phyllic alteration).(e) Biotite (Bt) altered to chlorite (Chl) and blue interference color epidote crystals (Ep) showing in monzogranites (Propylitic alteration).(d) High interference color of muscovite (Ms) flakes.(e) Phyllic alteration in rhyolites showing highly altered of large plagioclase (Pl).(f) Pyrite (Py) associated plagioclase and quartz in rhyolitic rocks.(e) Berlin blue color of well-developed zoisite (Zo) crystals in monzogranites along propylitic zone. (For interpretation of the references to color in this figure legend, the reader is referred to the web version of this article.)

Table 2
Distribution of the opaque minerals in the studied district.

Area	Sample No.	Petrographic nomenclature	Hematite	Magnetite	Titanomagnetite	Goethite	Martite	Rutile	Sulfides					Xenotime	Leucoxene	Uranothorite	Barite
									Pyrite	Arsenopyrite	Covellite	Galena	Chalcopyrite				
Wadi Khashir	K6	Red beds	xxxx	–	–	–	–	–	–	–	–	–	–	–	xxx	xxx	–
	K9		xxxx	–	–	–	–	–	–	–	–	–	–	–	xxx	xxx	–
	K35	Rhyolites	xxxx	–	–	x	–	x	xx	x	x	–	x	x	–	–	x
	K36	Listwaenites	–	xxxx	x	–	xxx	–	x	–	–	–	–	–	–	–	–
	K41	Sheared mineralized	x	–	–	x	–	x	xxxx	x	x	xx	xx	x	–	–	–
	K66	rhyolites	x	–	–	x	–	x	xxxx	x	x	xx	xx	x	–	–	–
	K71		x	–	–	x	–	x	xxx	x	x	–	xx	x	–		–
	K46	Fresh olivine-pyroxene	–	xxxx	xxxx	–	xxx	–	x	–	–	–	–	–	–	–	–
	K48	ferrogabbros	–	xxxx	xxxx	–	xxx	–	x	–	–	–	–	–	–	–	–
	K57	Quartzites	x	–	–	x	–	–	xxxx	x	x	x	x	xxx	–	–	–
	K59		x	–	–	x	–	–	xxxx	x	x	x	x	xx	–	–	–
	K70		x	–	–	x	–	–	xxxx	x	x	x	x	xx	–	–	–
Gabal Ras El-Kharit	R75	Arc- related metasediments	xx	–	–	xx	–	–	xxxx	–	x	–	–	xx	–	–	–
	R76		xx	–	–	xx	–	–	xxxx	–	–	–	–	xx	–	–	–
	R80	Sheared mineralized	xx	–	–	xx	–	xxx	xxx	x	x	xx	xx	xxx	–	–	xxx
	R81	rhyolites	xx	–	–	xx	–	xxx	xxx	x	x	xx	xx	xx	–	–	xxx
	R89	Rhyolites	x	–	–	x	–	x	xxxx	x	x	xx	x	xx	–	–	x
	R90	Pebbly-quartz- biotite schists	xxxx	–	–	–	–	–	x	–	–	–	–	–	–	–	–

(xxxx) = Dominant, (xxx) = Common, (xx) = Fairly common, (x) = Rare, (–) = Absent, (K) = Wadi Khashir, (R) = Gabal Ras El-Kharit.

special importance in locating different types of mineralization especially when they match well with the altered zones. Results of remote sensing data analysis (distribution of hydrothermal alteration and higher lineament density zones) were extensively checked through the detailed field and laboratory studies. We assume that the studied region, which is situated between the two shear zones (Kharit-Hodien and South Hafafit suture), was highly influenced by those two orogenies, resulting in the establishment of many shear zones (Fig. 1).

4.2. Fieldwork and analytical techniques

4.2.1. Fieldwork

A field investigation was carried out to confirm characteristics of alteration zones, structures, and lithological units. Intensive field study revealed that the metavolcanic can be divided into *meta*-andesites, metabasalts, and listvenite along the Ras El-Kharit area. The metasediments are classified as quartz-pyroxene schists, pebbly quartz-biotite schists, mylonitic schists, quartzites. Metagabbro-diorite-tonalite complex and younger felsic volcanics are distributed across the region. The monzogranite occurs in the central part of the area invaded by acidic and basic dykes. Coinciding with remote sensing results, several types of hydrothermal alterations (propylitic, phyllic, argillic, advanced argillic and oxidation alteration with local silicification) are detected through igneous and metamorphic rocks exposed mainly at the western part of the study area in (Fig. 8&9).

Propylitic alteration comprises mainly chlorite and epidote, together with lesser quantities of calcite, and zoisite. This alteration representing a low to intermediate temperatures (200–350 °C) and low fluid/rock ratios. The **phyllic alteration** is characterized by the complete substitution of the plagioclase feldspars by sericite. **Propylitic-phyllic alterations** are associated with granitic rocks, metasediments, metavolcanics and metagabbro-diorite-tonalite (Fig. 8a-d & 9a,d,e). **Argillic alteration** is characterized by the formation of the clay minerals. This alteration style is commonly subdivided into intermediate argillic and advanced argillic categories. **Intermediate argillic alteration** affects mainly plagioclase feldspars and is characterized by the formation of clay minerals (kaolinite). It typically forms below about 250 °C by H^+ metasomatism. **Advanced argillic alteration** represents an extreme form of base leaching where rocks have been stripped-off alkali elements by very acidic fluids active in high fluid/rock ratio environments. It is characterized by kaolinite, pyrophyllite, or dickite (depending on the temperature) and alunite together with some quartz, topaz, and tourmaline. Argillic and advanced argillic alterations are common in monzogranite. In the present region, **oxidation alteration zones** were discovered related to iron ore mineralization associated in metasediments (schists), rhyolite and the Samaday formation (Red sandstones) (Fig. 9e&f).

4.2.2. Petrography

Several alteration processes were found in the investigated region, affecting the Neoproterozoic basement rocks as well as the Phanerozoic rocks of the study area. Petrographic examinations of typical samples from these units revealed extensive **carbonatization, silicification, ferrugination (hematitization), kaolinitization, sericitization, chloritization, epidotization, muscovitization, pyritization, and zoisitization**.

The term **silicification** is used to indicate increased silica content as a result of metasomatic alteration (Pirajno, 2009a; Pirajno, 2009b). It was observed in different styles in tonalites, metagabbro-diorite, doleritic dykes, and listvenite (Fig. 10a). The **carbonatization** process refers to the alteration in rocks that result in the creation of calcium, magnesium, iron, and other metal carbonates. It can be found in various rock units of study areas, such as rhyolites and listvenite (Fig. 10a&b). **Ferrugination (i.e.** alteration associated with oxidizing fluids) often results in the formation of minerals with a high Fe^{3+}/Fe^{2+} ratio (Robb, 2005). The oxidation of ferrous iron into ferric iron, as well as the formation of goethite and hematite (Fig. 10b), is thought to be a key factor in this occurrence (Deimkov and Brogin, 1961; Langmuir, 1978). The ferrugination process was evidenced within the studied red beds of the Samaday Formation, sheared mineralized rhyolites, and pebbly quartz-biotite schists. **Kaolinitization** is a common process in argillic alteration and could be described as a transformation of aluminosilicates to kaolin in monzogranites (Fig. 10c). **Sericitization** observed in arc-related metasediments (after muscovite), metagabbro-diorite-tonalite complex (after plagioclase), rhyolites (after plagioclase and orthoclase), alkali feldspar granites (after plagioclase), and hornblende-biotite monzogranites occurs mainly in muscovite and plagioclase crystals (Fig. 10c,d&e). The **chloritization** process is recorded in listvenite, metaandesites, metabasalts, altered deformed diorites, quartz diorites, and monzogranites (Fig. 10e). The **muscovitization** process is observed after potassium feldspars and plagioclase crystals mainly in granitic rocks (Fig. 10f). **Epidotization** is recorded in *meta*-andesites, arc-related metasediments, metagabbro-diorite-tonalite complex, mylonites, rhyolites, spherulitic rhyolites, sheared mineralized rhyolites, and monzogranites (Fig. 10e&g). **Pyritization** (**sulphidation**) occurs mainly as large dissemination and along microfractures within the hydrothermal alteration zones of sheared mineralized rhyolites, quartzites, and arc-related metasediments (Fig. 10*h*). The **zoisitization** process is presented as alteration products within a plagioclase crystal observed in the metabasalt, metagabbros, tonalites, altered deformed diorites, fresh olivine-pyroxene ferrogabbros, rhyolites, spherulitic rhyolites, and monzogranites (Fig. 10i).

4.2.3. Ore microscopic investigation

To identify opaque minerals and their intergrowth and replacement textures, twenty samples of the studied rocks were examined using ore microscopy, X-ray diffraction (XRD), and EDAX analysis. A comprehensive investigation into the origins of ore and gangue minerals in rock samples from the present study was performed. The significant opaque minerals in the examined district are oxide (magnetite, martite, hematite, goethite, and rutile) and sulphide minerals (pyrite, arsenopyrite, and covellite) in the mineralized rock unites (Table 2). **Magnetite** occurs as euhedral to subhedral crystals of different sizes even in the same sample and it is iron-

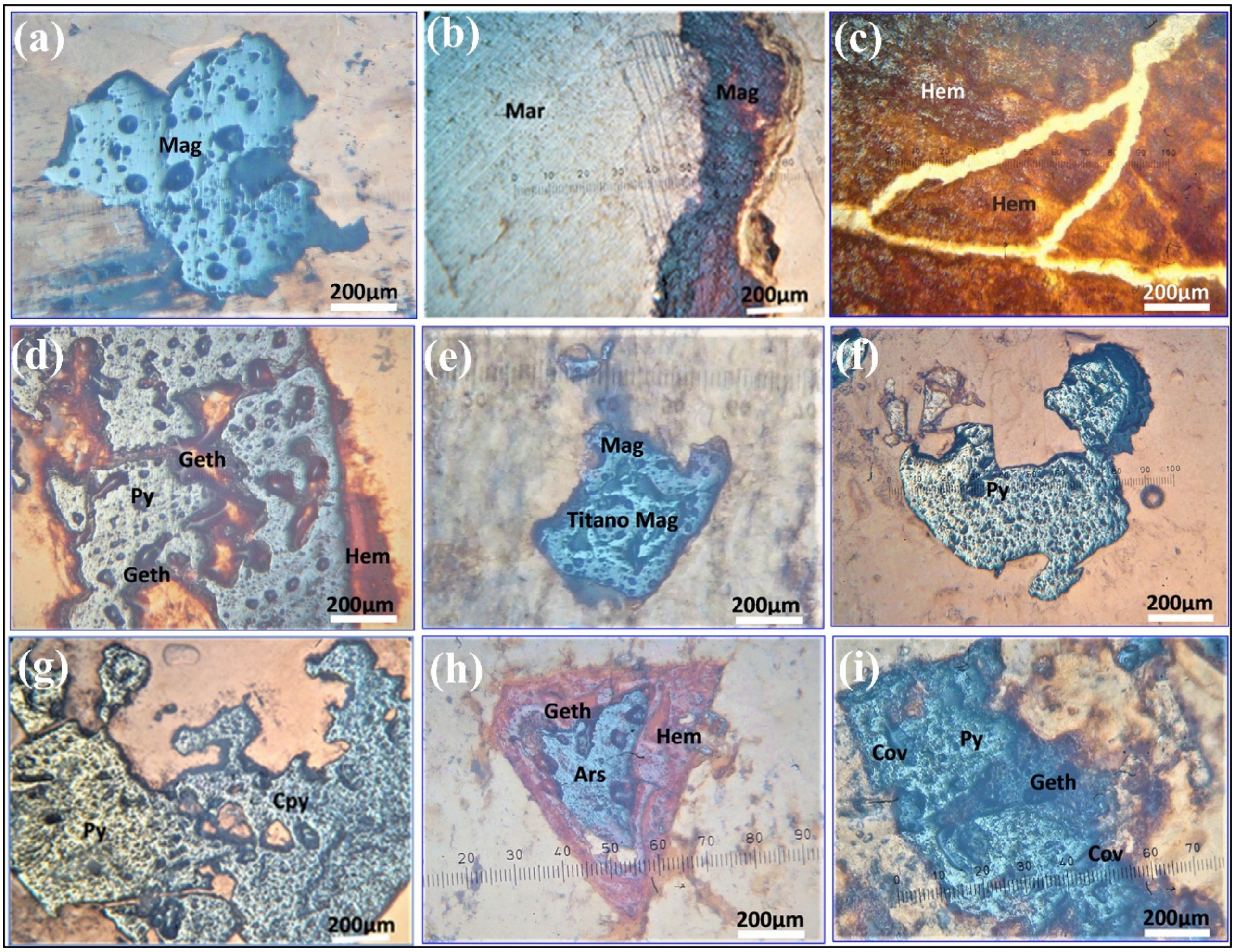

Fig. 11. Reflected light photomicrograph of opaque minerals showing: - **(a)** large magnetite (Mag) crystal enclosed within ferrogabbros (R.L. & K); **(b)** magnetite (Mag) crystals altered to martite (Mar) within the listwaenites (R.L. & K); **(c)** red hematite (Hem) crystal within red beds of Samaday Formation. (R.L. & K); **(d)** pyrite (Py) crystal oxidized to goethite (Geth) in the sheared mineralized rhyolites (R.L. & R); **(e)** subhedral titanomagnetite (Titan-Mag) crystals (R.L. & K); **(f)** irregular pyrite (Py) crystals within quartzites (R.L. & K); **(g)** anhedral pyrite (Py) crystal replacement in chalcopyrite (Cpy) in the sheared mineralized rhyolites (R.L. & R); **(h)** arsenopyrite (Ars) crystal oxidized to goethite (Geth) and hematite (Hem) within sheared mineralized rhyolites (R.L. & R); **(i)** pyrite (Py) crystals exsolution within anhedral blue covellite (Cov) crystals and also oxidized to goethite (Geth; R.L. & R). (For interpretation of the references to color in this figure legend, the reader is referred to the web version of this article.)

black to reddish-brown in color with a metallic luster. Magnetite crystals are included within the Wadi Khashir fresh olivine-pyroxene ferrogabbros and listvenite (Fig. 11a). The total amount of magnetite crystals ranges from 50 to 53 w% of the fresh olivine-pyroxene ferrogabbros at Wadi Khashir area. **Martite** occurs as lamellar, radial, or prismatic crystals, generally grey to light bluish grey (Fig. 11b). Magnetite partially to completely altered to martite that occurs as a secondary mineral due to the oxidation of magnetite within the ferruginated shear zones and iron-bearing listvenite. **Hematite** occurs in a variety of different forms. It fills the fractures and interspaces between crystals in the hand specimen (Fig. 11c). Hematite exhibits moderate relief, parallel and sharp extinction in Wadi Khashir red beds of Samaday Formation (Fig. 11c). It occurs as irregular aggregates exhibiting white color and cherry red internal reflection. Sometimes, it is bounded by goethite and limonite owing to its hydration effect (Fig. 11d). The ore microscopic studies recorded that hematite iron ore is the main component of the red-colored beds. **Titanomagnetite** appears as medium-grained, euhedral, irregular crystals and exsolution of fine network intergrowth of titanomagnetite within euhedral magnetite crystals with porphyroblastic texture (Fig. 11e). **Pyrite** was found as yellow to yellowish white in color, high relief, scattered grains within Wadi Khashir - Gabal Ras El-Kharit rock units (Fig. 11f). Also, pyrite appears as euhedral to subhedral and triangular crystals, and it may form well-formed cubic and pyramidal crystals (Fig. 11g); moreover, it occurs as independent disseminated shreds, anhedral crystals, and very fine grains within the hydrothermal alteration zones of the study district. **Chalcopyrite** is presented as a minor component in the sheared mineralized rhyolites and it replaces the pyrite (Fig. 11g). Chalcopyrite also occurs as minor, very fine exsolution lamellae in pyrite. Both pyrite and chalcopyrite often have irregular cracks and a cataclastic texture indicating shear movement along the ore-bearing microfracture zones. **Arsenopyrite** occurs as white to faint yellow tint with pleochroism from white with a bluish tint to faint reddish yellow, blocky, and granular grains. Sometimes, it occurs as exsolution within pyrite crystals (Fig. 11*h*). Arsenopyrite occurs as inclusions in the alteration zones of the sheared mineralized rhyolites at Gabal Ras El-Kharit - Wadi Khashir district. **Covellite** has brilliant indigo-blue to light blue in color, and appears as anhedral to subhedral crystals, large striated hexagonal plates, foliated, massive, with strong pleochroism from deep blue to blue-grey, and strong anisotropy (Fig. 11i). Occasionally, it can be found in hydrothermal alteration zones of sheared mineralized rhyolites at Gabal Ras El-Kharit area. **Goethite** occurs as an oxidation product of pyrite and chalcopyrite. or secondary minerals replacing other constituents, such as pyrite and chalcopyrite crystals (Fig. 11*h*&i).

4.2.4. Mineralogy of the studied hydrothermally altered rocks (XRD)

The identified minerals can be classified into two groups from the point of view of the present work as ore minerals and associated gangue minerals. The investigated X-ray diffraction patterns of fresh olivine-pyroxene ferrogabbros, and quartzite (Fig. 12a&b) show that they are mainly composed of **magnetite, hematite, and quartz**, while, sheared mineralized rhyolites and arc-related metasediments contain **pyrite, galena, rutile,** and **quartz** (Fig. 12c&d). The X-ray diffraction analyses of heavy fractions for

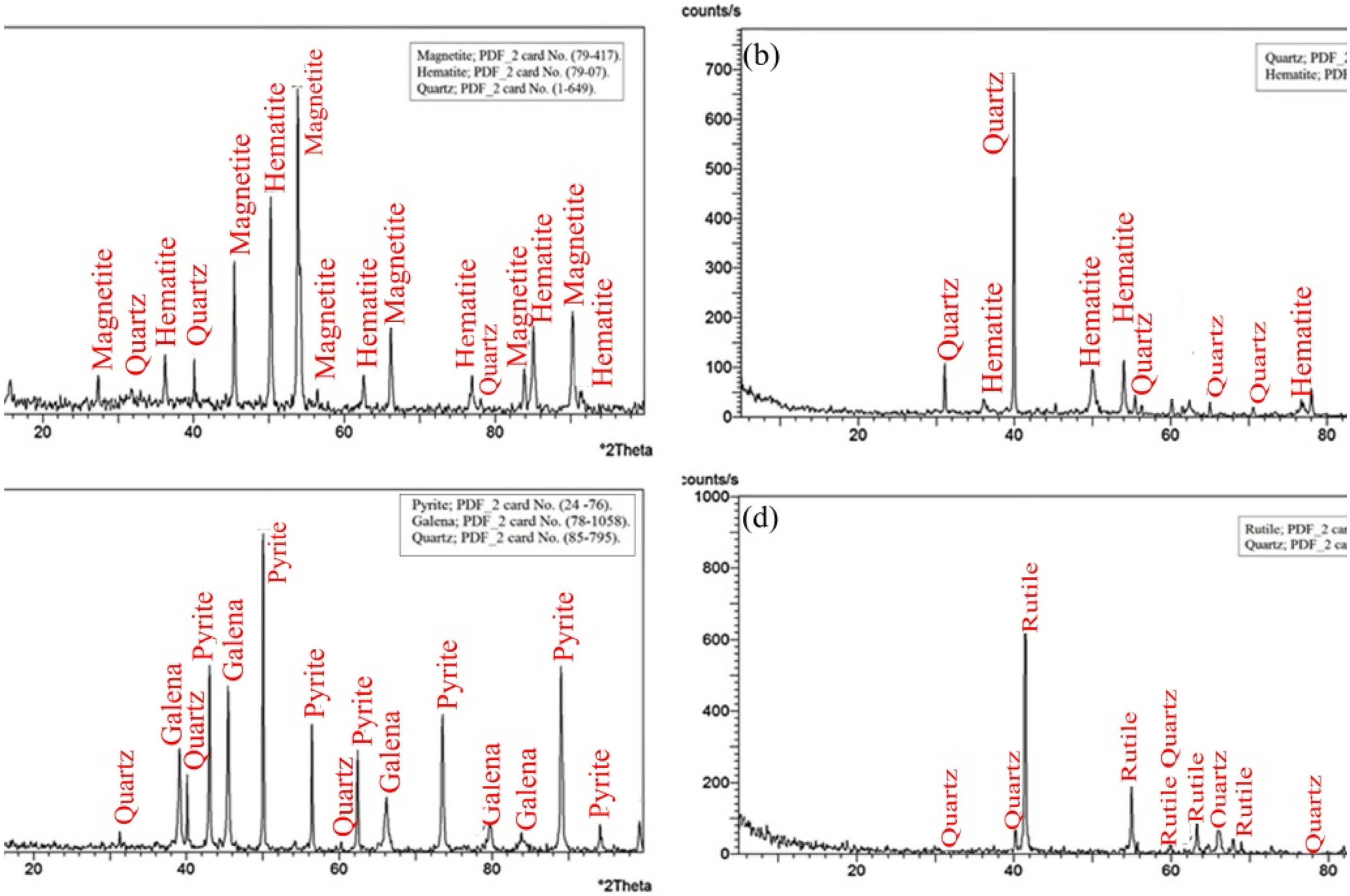

Fig. 12. X-ray diffraction patterns of the studied rocks.

the studied samples were confirmed by the ore microscopic investigations and EDX analyses of SEM.

4.2.5. Scanning electronic microscopy and EDX analysis

Back-scattered electron (BSE) images display some of the textural characteristics of the study ore-bearing rock units. Sulfide and oxide minerals of the study area occur within the metavolcanics, arc-related metasediments, fresh olivine-pyroxene ferrogabbros, younger felsic volcanics, and the red-colored beds of the Samaday Formation. Disseminated sulphide minerals (dark brown, black to yellow in color) associated with hydrothermally altered zones of sheared mineralized rhyolites and arc-related metasediments. While, the oxide minerals are associated with listvenite, fresh olivine-pyroxene ferrogabbros and red beds.

Magnetite, titanomagnetite, hematite, goethite, pyrite, xenotime, galena, rutile, and barite have all been discovered using a scanning electron microscope in thin polished sections from the present region.

Magnetite represents coarse-grained crystals in listvenite as can be seen in Fig. 13a. The X-ray spectrum of magnetite in the listvenite shows a high Fe peak (75.32 %). Disseminated **titanomagnetite** ores are situated in olivine-pyroxene ferrogabbros. EDX analyses of titanomagnetite display high peaks of iron (68.74 %) and titanium (16.61 %) (Fig. 13 b). **Hematite** grains are disseminated in the red beds of the Samaday Formation showing a high iron peak (67.35 %; Fig. 13 c). EDX analyses of **pyrite** crystals spotted within the hydrothermal alteration zones in sheared mineralized rhyolites and arc-related metasediments. These analyses display high peaks of sulfur (57.97 %) and iron (42.03 %) (Fig. 13 d).

Xenotime crystals appear as short to long prismatic and equant. Figure (14 a) shows the EDX analyses of xenotime crystals within the quartzites and sheared mineralized rhyolites. EDX analyses of **rutile** grains encountered in the sheared mineralized rhyolites display high peaks of titanium (57.97 %), oxygen (34.79 %), and Si (4.60 %) (Fig. 14 b). Fig. 13a shows the results of EDX analyses on **galena** grains recorded in the sheared mineralized rhyolites. According to this figure, the Pb content in galena reaches 91.9 % (Fig. 14 c). The quantitative data of analyzed **barite** grains within the hydrothermal alteration zones and the sheared mineralized rhyolites show 54.42 % Ba, 16.91 % S, 16.04 % Fe, 5.06 % Si, and 0.61 % K content (Fig. 14 d).

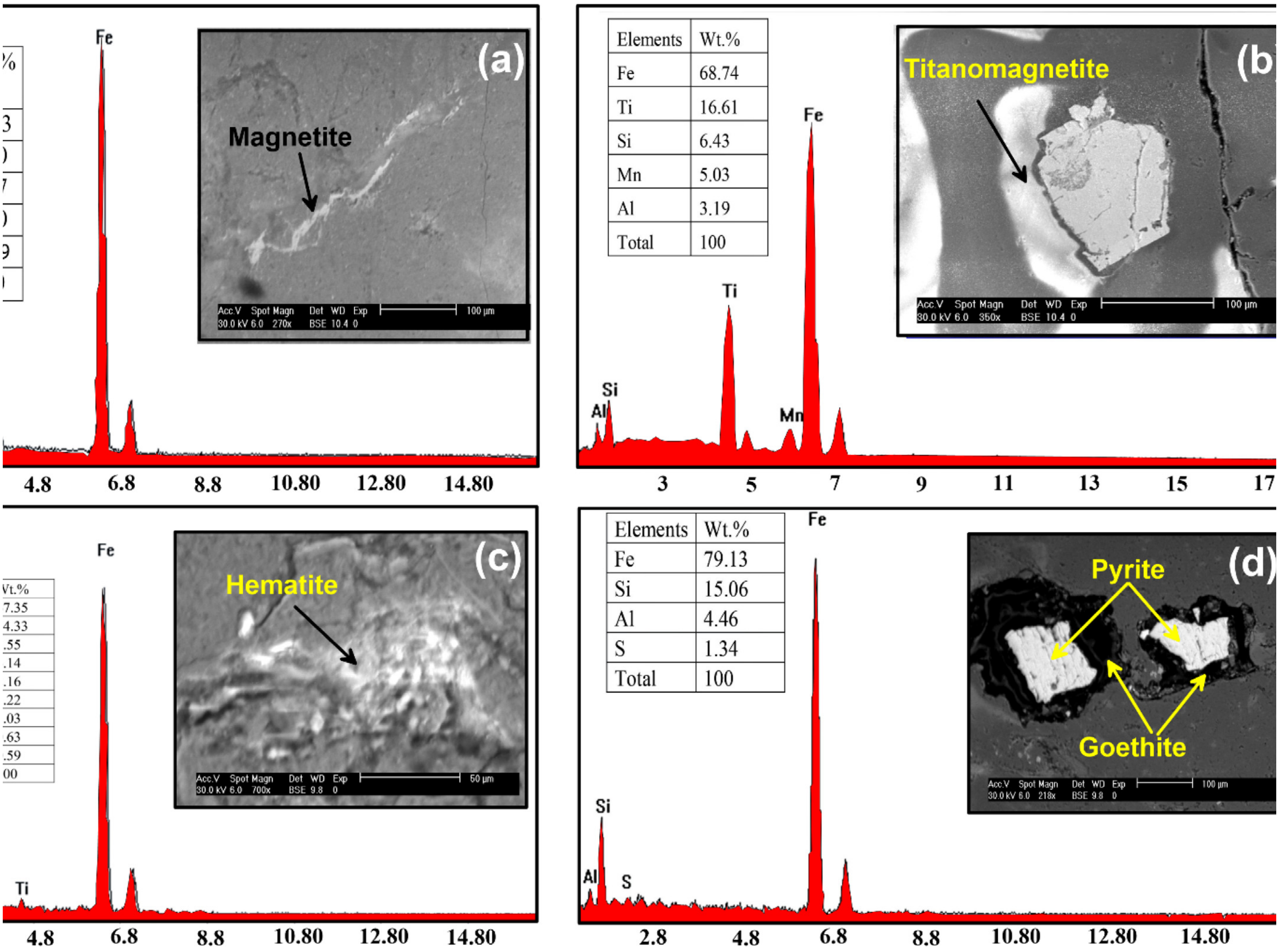

Fig. 13. BSE image and EDX spot analyses showing: **(a)** magnetite grains disseminated in the studied listvanites; **(b)** titanomagnetite grains in the studied fresh olivine-pyroxene ferrogabbros; **(c)** hematite grains disseminated in the studied mineralized red beds of Samady Formation; **(d)** pyrite grains altered to goethite in the studied sheared mineralized rhyolites. (For interpretation of the references to color in this figure legend, the reader is referred to the web version of this article.)

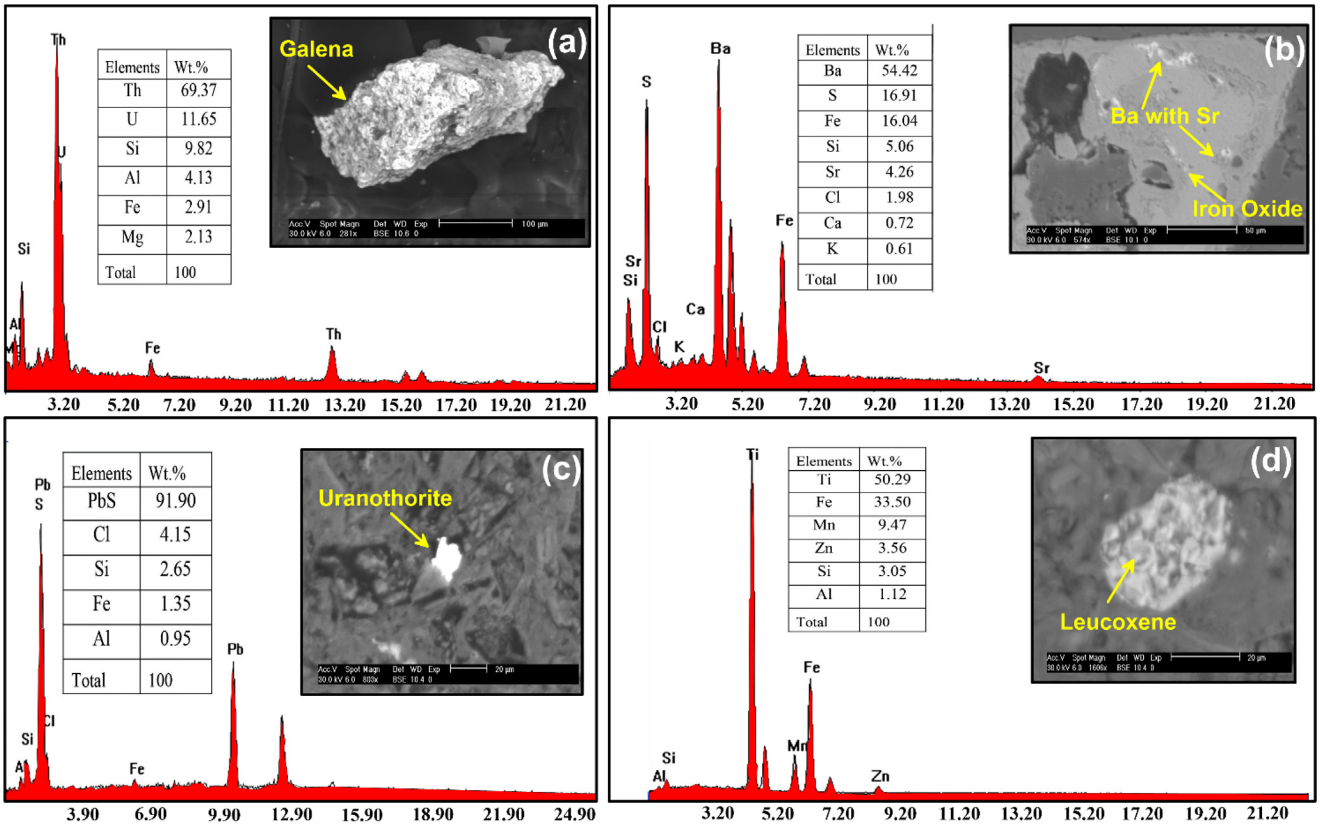

(a)

Elements	Wt.%
Th	69.37
U	11.65
Si	9.82
Al	4.13
Fe	2.91
Mg	2.13
Total	100

(b)

Elements	Wt.%
Ba	54.42
S	16.91
Fe	16.04
Si	5.06
Sr	4.26
Cl	1.98
Ca	0.72
K	0.61
Total	100

(c)

Elements	Wt.%
PbS	91.90
Cl	4.15
Si	2.65
Fe	1.35
Al	0.95
Total	100

(d)

Elements	Wt.%
Ti	50.29
Fe	33.50
Mn	9.47
Zn	3.56
Si	3.05
Al	1.12
Total	100

Fig. 14. BSE image and EDX spot analyses showing: **(a)** xenotime grains in the studied mineralized arc-related metasediment rocks; **(b)** rutile grains in the studied sheared mineralized rhyolites; **(c) galena** grains in the studied sheared mineralized rhyolites; **(d) barite** grains enclosed in **iron oxides** in the studied sheared mineralized rhyolites.

5. Discussions

5.1. Paragenetic sequence of the mineral deposits

The paragenetic sequence of Wadi Khashir and Gabal Ras El-Kharit mineralization shows early metamorphic minerals of the arc-related metasediments and late sulfides deposited from hydrothermal solutions migrated from the Wadi Khashir and Gabal Ras El-Kharit granitic intrusions and extrusive younger felsic volcanics (Table 3). The early metamorphic mineral deposits are characterized by low- to medium-grade regional metamorphism of greenschist facies, while irregular patches, veinlets and disseminated textures, characterize the late sulfide ores. The sulfide deposits have formed due to the latter process, which results in the formation of pyrite, chalcopyrite, arsenopyrite, galena, and covellite, mainly. These sulfides occur as disseminated ore mineralization characterized by small, scattered patches and relatively simple mineralogy. Most of the sulfides were altered to secondary oxide minerals by supergene enrichment process, such as goethite.

5.2. Mineral potentiality mapping

Hydrothermal alteration results, structural analysis findings, fieldwork shreds of evidence, the spatial distribution of the detected ore samples were collectively gathered in a GIS environment to build a Mineral Potentiality Map (MPM). Firstly, results of hydrothermal alterations extracted by using ASTER and Sentinel 2 data were visually interpreted in their geological context to exclude the results that mostly highlight weathering and confirm those which related to hydrothermal events. For example, most of the detected anomalies over alkali feldspar granites are mainly due to the weathering, unlike those concentrated mainly around ferrogabbro and metavolcanics, closer to Gabal Ras El Kharit-Gabal Khasir zone. Similarly, lithological units characterized mainly by hydrothermal alterations are assigned through intensive field survey and rock samples investigations. In the same way, density maps of lineaments highlight intensively dissected areas.

Practically, MPM was built after spatial overlay analysis of several layers including hydrothermal alterations, representative samples bearing mineralization, and structurally dissected zones. Visual interpretation and supervision were a must to build efficient MPM because the same layer (for example, hydrothermal alteration) may guide to a mineral potential zone or just indicate a surface weathering process (misguidance). Consequently, a different approach for building the MPM was adopted in the current study through a grid of well-distributed points over the study area (more than 50 points were utilized). For each point, five main factors were considered (structural complexity, ASTER alteration result, Sentinel-2 alteration result, field verification for alterations (real alteration zone), and representative samples). Basically, these factors were given the same weight (importance) without any preferences as favorable mineralized zones are mostly controlled by a structural regime and associated with one or more alteration types. For instance, if the point has a considered structural complexity (1), ASTER alteration result (1), Sentinel 2 alteration result (1), verified alteration zones (1), and representative mineralized sample (1), then the sum of these weights is (5), meaning that this point has very high potentiality for mineralization. Similarly, if any of

Table 3
Paragenetic sequence of the mineral deposits in the Wadi Khashir and Gabal Ras El-Kharit rock units.

Mineral deposits	Stages of mineralization			
	Metamorphism stage	Magmatic stage	Hydrothermal stage	Supergene stage
Magnetite		▬		
Titanomagnetite		▬		
Martite				▬
Hematite			▬	
Galena			▬	
Cerussite				▬
Pyrite			▬	
Chalcopyrite			▬	
Arsenopyrite			▬	
Covellite			▬	
Goethite				▬
Barite		▬		
Xenotime	▬			
Rutile		▬		
Uranothorite				▬
Leucoxene				▬
Chlorite	▬			
Calcite	▬		▬	
Magnesite	▬		▬	
Sericite	▬		▬	
Epidote	▬		▬	
Zoisite	▬		▬	

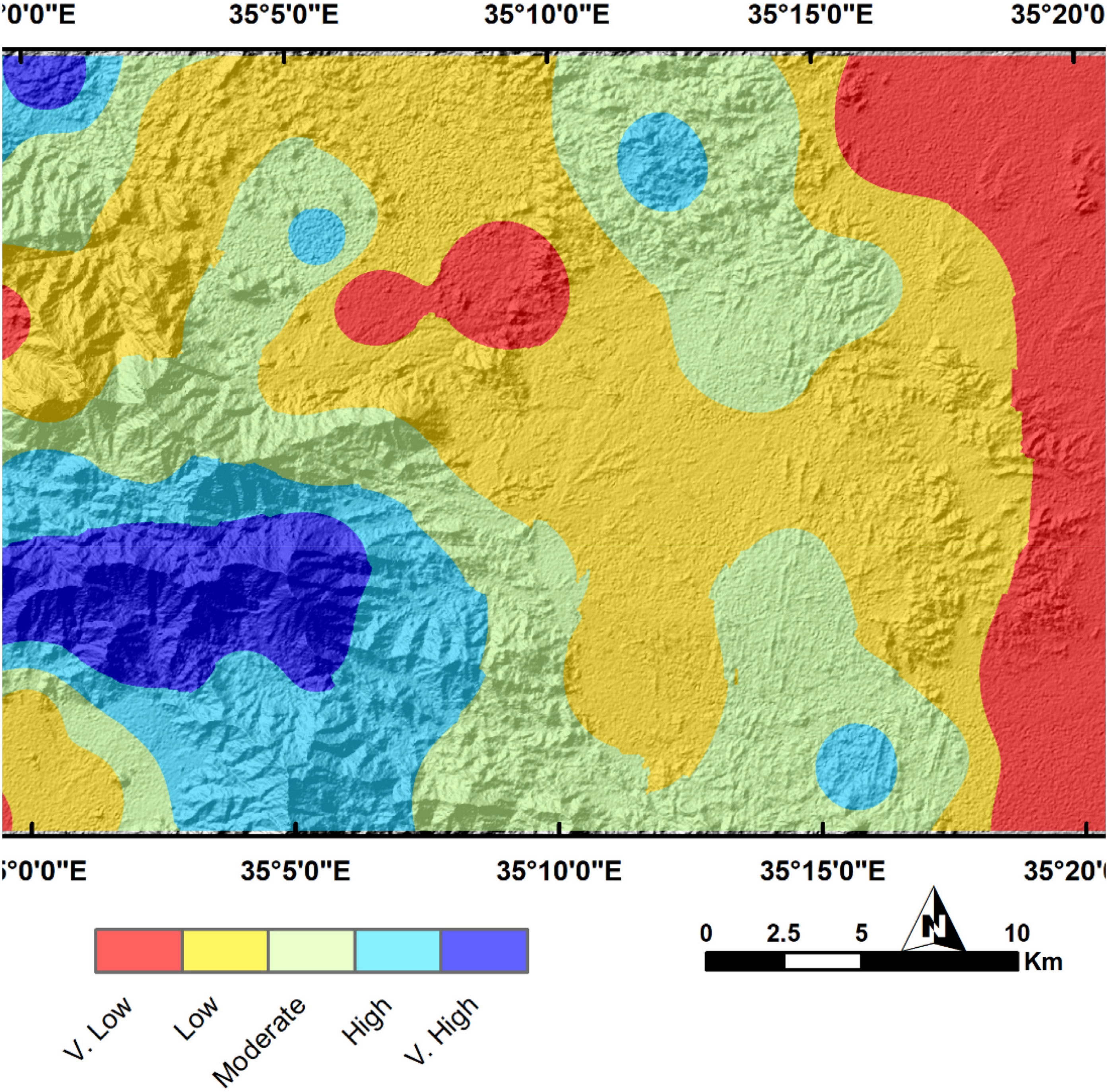

Fig. 15. Mineral Potentiality Map of the study area.

these elements are missed at another point, then the total weight is considered as (4) indicating that the mineral potentiality at this point is high. So, over a scale from (1) to (5), each point has a certain weight ranging from 1 (very low) to 5 (very high) using a simple additive method as shown in the final MPM.

Through this weighted overlay analysis (simple additive method) (Shebl et al., 2021), an MPM was constructed (Fig. 15) highlighting a considered part of the study area possessing higher potentiality (mostly real alteration anomalies over highly dissected areas). It should be emphasized that most of these favorable mineralized zones are confirmed by intensive fieldwork and petrographic study.

6. Conclusions

1. Sentinel 2 and ASTER datasets reasonably allocate different types of hydrothermal alterations that mostly coincide with those verified through fieldwork. ALOS PALSAR DEM is efficient in extracting linear structural features.
2. Through detailed petrographic analysis, the main detected alteration minerals are chlorite, epidote, hematite, zoisite, kaolinite, pyrite, sericite, muscovite, and calcite.
3. Hydrothermally altered rhyolites occasionally contain high amounts of iron oxides and sulfides.

4. The essential alteration types are sericitization, sulphidation, ferrugination, and carbonatization.
5. Two metamorphic grades are identified within the study area: high-grade regional metamorphism and a slightly low-grade zone.
6. Integrated remote sensing techniques, field studies, petrography, and mineralogy of the mineralization and alteration zones are extremely useful to build a verified mineral potentiality map of the study area.
7. MPM highlights an area of approximately 125 km^2 as a higher potential zone for various mineralizations. The latter are mainly represented by pyrite, magnetite, titanomagnetite, hematite, chalcopyrite, arsenopyrite, covellite, galena, cerussite, rutile, martite, goethite, barite, zircon, xenotime, uranothorite, and leucoxene. These mineralizations are hosted mainly in the sheared mineralized rhyolites, ferrogabbros, and arc-related metasediments.

Declaration of Competing Interest

The authors declare that they have no known competing financial interests or personal relationships that could have appeared to influence the work reported in this paper.

Acknowledgments

The authors deeply thank Prof. Rózsa Péter (University of Debrecen) for his efforts in revising this manuscript to be in the current form.Great thanks to ESA and USGS for providing the remote sensing data. Ali Shebl is funded by Stipendium Hungaricum scholarship under the joint executive program between Hungary and Egypt.

References

Abd El-Wahed, M.A., 2014. Oppositely dipping thrusts and transpressional imbricate zone in the Central Eastern Desert of Egypt. J Afr Earth Sci 100, 42–59 https://www.researchgate.net/publication/263551813.

Abd El-Wahed, M., Zoheir, B., Pour, A.B., Kamh, S., 2021. Shear-related gold ores in the Wadi Hodein Shear Belt, South Eastern Desert of Egypt: analysis of remote sensing, field and structural data. Minerals 11 (5), 474.

Abdelmalik, K.W., 2019. Landsat 8: Utilizing sensitive response bands concept for image processing and mapping of basalts. Egypt. J. Rem. Sens. Space Sci. 23 (3), 263–274.

Aboelkhair, H., Ninomiya, Y., Watanabe, Y., Sato, I., 2010. Processing and interpretation of ASTER TIR data for mapping of rare-metal-enriched albite granitoids in the Central Eastern Desert of Egypt. J. African Earth Sci. 58, 141–151. https://doi.org/10.1016/j.jafrearsci.2010.01.007.

Azizi, H., Tarverdi, M.A., Akbarpour, A., 2010. Extraction of hydrothermal alterations from ASTER SWIR data from east Zanjan, northern Iran. Adv. Space Res. 46, 99–109. https://doi.org/10.1016/j.asr.2010.03.014.

de Wall, H., Greiling, R.O., Sadek, M.F., 2001. Post-collisional shortening in the late Pan-African Hamisana high strain zone, SE Egypt: field and magnetic fabric evidence. Precambr. Res. 107, 179–194. https://doi.org/10.1016/s0301-9268(00)00141-8.

Deimkov, Y.V., Brogin, B.V., 1961. On coloring of minerals in uranium-bearing veins. At. Energ. n-1, 13–19.

EGSMA, 1997. Geological Survey of Egypt, Geological map of Egypt, Scale 1:250,000, NG 36 D Sheet.

El Ghrabawy, O., Soliman, N., Tarshan, A., 2019. Remote sensing signature analysis of ASTER imagery for geological mapping of Gasus area, central eastern desert, Egypt. Arab. J. Geosci. 12 (13). https://doi.org/10.1007/s12517-019-4531-9.

El-Desoky, H.M., Soliman, N., Heikal, M.A., Abdel-Rahman, A.M., 2021. Mapping hydrothermal alteration zones using ASTER images in the Arabian-Nubian Shield: A case study of the northwestern Allaqi District, South Eastern Desert, Egypt. J. Asian Earth Sci.: X 5,. https://doi.org/10.1016/j.jaesx.2021.100060 100060.

El-Hadidy, S.M., Alshehri, F., Sahour, H., Abdelmalik, K.W., 2022. Detecting hydrocarbon micro-seepage and related contamination, probable prospect areas, deduced from a comparative analysis of multispectral and hyperspectral satellite images. J. King Saud Univers. – Sci. 34 (6), 102192.

El-Kazzaz, Y.A., 2010. Geometry of fold interference patterns in Wadi Kharit area, South Eastern Desert, Egypt. Egypt. J. Rem. Sens. Space Sci. 13 (2), 113–120. https://doi.org/10.1016/j.ejrs.2010.12.001.

Emam, A., Zoheir, B., Johnson, P., 2016. ASTER-based mapping of ophiolitic rocks: Examples from the Allaqi-Heiani suture, SE Egypt. Int. Geol. Rev. 58, 525–539. https://doi.org/10.1080/00206814.2015.1094382.

Farag, K.S.I., Howari, F.M., Abdelmalik, K.W., 2019. Imaging of hydrothermal altered zones in Wadi Al-Bana, in southern Yemen, using remote sensing techniques and very low frequency–electromagnetic data. Arab. J. Geosci. 12 (18).

Fossi, D.H., Djomo, H.D., Takodjou Wambo, J.D., Kouayep Tchoundi, L.C., Deassou Sezine, E., Takam Tchoupe, G.B., Tchatchueng, R., 2021. Extraction and analysis of structural lineaments from Mokolo area, North Cameroon, using DEM and remote sensing images, and their influence on drainage morphometric. Arabian J. Geosci. 14 (19), 1–14.

Fowler, A., Baghdady, A., Abdelmalik, K., Gad, A., 2020. Remote sensing-guided stratigraphic dissection of an Ediacaran terrestrial molasse basin (Kareim basin, Egypt), with implications for sedimentary evolution. Precambr. Res. 338,. https://doi.org/10.1016/j.precamres.2019.105589 105589.

Fritz, H., Wallbrecher, E., Khudier, A.A., Abu El Ela, F., Dallmeyer, R.D. (1996) Formation of Neoproterozoic metamorphic core complexes during oblique convergence, Eastern Desert, Egypt. J. Afr. Earth Sci. 23:311–329. PIh S0899-5362(97)00004“3.

Gabr, S., Ghulam, A., Kusky, T., 2010. Detecting areas of high-potential gold mineralization using ASTER data. Ore Geol. Rev. 38, 59–69. https://doi.org/10.1016/j.oregeorev.2010.05.007.

Gad, S., Kusky, T., 2006. Lithological mapping in the Eastern Desert of Egypt, the Barramiya area, using Landsat thematic mapper (TM). J. African Earth Sci. 44, 196–202. https://doi.org/10.1016/j.jafrearsci.2005.10.014.

Goetz, A.F.H., 2009. Three decades of hyperspectral remote sensing of the Earth: A personal view. Remote Sens. Environ. 113, S6–S16. https://doi.org/10.1016/j.rse.2007.12.014.

Greiling, R.O., Abdeen, M.M., Dardir, A.A., El-Akhal, H., El-Ramly, M.F., Kamal El Din, G.M., Osman, A.F., Rashwan, A.A., Rice, A.H., Sadek, M.F., 1994. A structural synthesis of the Proteorozoic Arabian-Nubian Shield in Egypt. Geol Rundsch 83, 484–501. https://doi.org/10.1007/bf01083222.

Greiling, R.O., de Wall, H., Warr, L.N., Naim, G.M., Hussein, A.A., Sadek, M.F., Abdeen, M.M., El Kady, M.F., Makhlouf, A., 1996. Basement structure in Eastern Egypt: quantitative perspectives for the second century. Proc. Geol. Surv. Egypt Cenn. Conf., 289–302

Hamimi, Z., Abd El-Wahed, M., Gahlan, H.A., Kamh, S.Z. 2019 Tectonics of the Eastern Desert of Egypt: key to understanding the Neoproterozoic evolution of the Arabian-Nubian Shield (East African Orogen). In: Bendaoud A, Hamimi Z, Hamoudi M, Djemai S, Zoheir B (eds) Geology of the Arab World—an Overview, Springer Geology, 1–81. Doi: 10.1007/978-3-319-96794-3_1.

Kennedy, C., 1964. Induced bias in innovation and the theory of distribution. Econ. J. 74 (295), 541–547. https://doi.org/10.2307/2228295.

Ketchaya, Y.B., Dong, G., Fotze, Q.M.A., Carrino, T.A., Mandeng, E.P.B., Lemdjou, Y.B., Assie, K., Fodoue, Y., J & Wassouo Wadjou, J, 2021. Integration of Landsat 8, gravity, and field data for exploration of gold mineralization in Gamba District, Northern Cameroon. Geol. J. 56 (9), 4788–4808.

Lamri, T., Djemaï, S., Hamoudi, M., Zoheir, B., Bendaoud, A., Ouzegane, K., Amara, M., 2016. Satellite imagery and airborne geophysics for geologic mapping of the Edembo area, Eastern Hoggar (Algerian Sahara). J. Afr. Earth. Sci. 115, 143–158. https://doi.org/10.1016/j.jafrearsci.2015.12.008.

Langmuir, D., 1978. Uranium-solution mineral equilibria at low temperatures with applications to sedimentary ore deposits. Geochim. Cosmochim. Acta 42 (6), 547–569. https://doi.org/10.1016/0016-7037(78)90001-7.

Mbianya, G.N., Ngnotue, T., Wambo, J.D.T., Ganno, S., Pour, A.B., Kenne, P.A., Fossi, D. H., Wolf, I.D., 2021. Remote sensing satellite-based structural/alteration mapping for gold exploration in the Ketté goldfield, Eastern Cameroon. J. Afr. Earth. Sci. 184, 104386.

Nguemhe Fils, S.C., Mimba, M.E., Nyeck, B., Nforba, M.T., Kankeu, B., Njandjock Nouck, P., Hell, J.V., 2020. GIS-based spatial analysis of regional-scale structural controls on gold mineralization along the Betare-Oya Shear Zone, Eastern Cameroon. Natl. Resour. Res. 29 (6), 3457–3477.

Pirajno, F., 2009b. Hydrothermal processes and wall rock alteration. In: Hydrothermal Processes and Mineral Systems. Springer, Dordrecht, pp. 73–164.

Pirajno, F. (2009) Hydrothermal Processes and Mineral Systems, Springer-Verlag, 1241. 1273 стр., ISBN: 978-1-4020-8612-0.

Rajesh, H.M., 2004. Application of remote sensing and GIS in mineral resource mapping-An overview. J. Mineral. Petrol. Sci. 99 (3), 83–103. https://doi.org/10.2465/jmps.99.83.

Ramadan, T.M., Abdelsalam, M.G., Stern, R.J., 2001. Mapping gold-bearing massive sulfide deposits in the Neoproterozoic Allaqi suture, SE Egypt with Landsat TM and SIRC/X-SAR images. J. Photogrammet. Eng. Rem. Sens. 67 (4), 491–497.

Robb, L.J., 2005. Introduction to Ore-Forming Processes. Blackwell Publishing Company.

Sabins, F.F., 1999. Remote sensing for mineral exploration. Ore Geol. Rev. 14, 157–183. https://doi.org/10.1016/S0169-1368(99)00007-4.

Salem, S.M., Soliman, N.M., 2015. Exploration of gold at the east end of Wadi Allaqi, South Eastern Desert, Egypt, using remote sensing techniques. Arabian J. Geosci. 8 (11), 9271–9282. https://doi.org/10.1007/s12517-015-1880-x.

Shebl, A., Csámer, Á., 2021a. Lithological, structural and hydrothermal alteration mapping utilizing remote sensing datasets: a case study around Um Salim area. Egypt. IOP Conf. Ser. Earth Environ. Sci. 942,. https://doi.org/10.1088/1755-1315/942/1/012032 012032.

Shebl, A., Csámer, Á., 2021b. Reappraisal of DEMs, Radar and optical datasets in lineaments extraction with emphasis on the spatial context. Remote Sens. Appl. Soc. Environ. 24,. https://doi.org/10.1016/J.RSASE.2021.100617 100617.

Shebl, A., Csámer, Á., 2021c. Stacked vector multi-source lithologic classification utilizing Machine Learning Algorithms: Data potentiality and dimensionality monitoring. Remote Sens. Appl. Soc. Environ. 24, 100643.

Shebl, A., Abdellatif, M., Elkhateeb, S.O., Csámer, Á. 2021 Multisource Data Analysis for Gold Potentiality Mapping of Atalla Area and Its Environs, Central Eastern Desert, Egypt. Miner. 2021,11,641 11, 641. https://doi.org/10.3390/MIN11060641.

Stern, R.J., Hedge, C.E., 1985. Geochronologic constraints on late Precambrian crustal evolution in the Eastern Desert of Egypt. Am. J. Sci. 285, 97–127.

Traore, M., Wambo, J.D.T., Ndepete, C.P., Tekin, S., Pour, A.B., Muslim, A.M., 2020. Lithological and alteration mineral mapping for alluvial gold exploration in the south east of Birao area, Central African Republic using Landsat-8 Operational Land Imager (OLI) data. J. Afr. Earth. Sci. 170, 103933.

Wambo, J.D.T., Ganno, S., Ngambu, A.A., Negue, E.N., Ondoa, J.M., Nzenti, J.P., 2016. Use of landsat 7 ETM+ Data for the geological structure interpretation: case study of the Ngoura-Colomines Area, Eastern Cameroon. J. Geosci. 4 (3), 61–72.

Wambo, J.D.T., Pour, A.B., Ganno, S., Asimow, P.D., Zoheir, B., dos Reis Salles, R., Nzenti, J., Pradhan, B., Muslim, A.M., 2020. Identifying high potential zones of gold mineralization in a sub-tropical region using Landsat-8 and ASTER remote sensing data: a case study of the Ngoura-Colomines goldfield, eastern Cameroon. Ore Geol. Rev. 122, 103530.

Zhang, X., Pazner, M. 2007 Comparison of Lithologic Mapping with ASTER, Hyperion, and ETM Data in the Southeastern Chocolate Mountains, USA. Photogramm. Eng. Remote Sens. 73(5):555-561 Doi: 10.14358/PERS.73.5.555.

Zoheir, B., Emam, A., Abdel-Wahed, M., Soliman, N., 2019. Multispectral and radar data for the setting of gold mineralization in the South Eastern Desert. Egypt. Remote Sensing. Remote Sensing 11 (12), 1450. https://doi.org/10.3390/rs11121450.

Further reading

Ford, j.H., Green, D.C. 1977 An oxygenand hydrogenisotope study of the Panguna porphyry-copper deposit, Bougainville. Australian J. Earth Sci., 24 (1), 63-80 Doi: 10.1080/00167617708728967.

Hall, A., 1993. The influence of secondary alteration on the ammonium content of granites, exemplified by the Rosses Complex of Donegal. Mineral. Mag. 57 (389), 591–598. https://doi.org/10.1180/minmag.1993.057.389.03.

Harlov, D.E., Austrheim, H., 2013. Metasomatism and the Chemical Transformation of Rock: The Role of Fluids in Terrestrial and Extraterrestrial Processes. Springer 789. https://doi.org/10.1007/978-3-642-28394-9.

Mathieu, L., 2016. Quantifying hydrothermal alteration with normative minerals and other chemical tools at the Beattie Syenite, Abitibi greenstone belt. Canada. Geochem Explor. Environ. Anal. 16, 233–244. https://doi.org/10.3390/geosciences8070245.

Monier, G., Mergoil-Daniel, J., Labernardiere, H., 1984. Générations successives de muscovites feldspaths potassiques dans les leucogranite du massif de Millevaches (Massif Central francais). Bull. Minéral. 107, 55–68.

Munha, J., Fyfe, W.S., Kerrich, R., 1980. Adularia, the characteristic mineral of felsic spilites. Contrib. Miner. Petrol. 75, 15–19.

Ridley, J. 2013 Ore Deposit Geology. Cambridge University Press., 398. Doi: 10.1017/CBO9781139135528

Walshe, J.L., 1986. A six-component chlorite solid solution model and the conditions of chlorite formation in hydrothermal and geothermal systems. Econ. Geol. 81 (3), 681–703. https://doi.org/10.2113/gsecongeo.81.3.681.